**Enhancing Light-matter Interaction in Ultrathin Films
using Optical Nanostructures**

by

Wenyi Wang

Dissertation

Submitted to the Faculty of the

Graduate School of Vanderbilt University

in partial fulfillment of the requirements

for the degree of

DOCTOR OF PHILOSOPHY

in

Electrical Engineering

May, 2016

Nashville, Tennessee

Approved:

Jason G. Valentine, Ph.D.

Sharon M. Weiss, Ph.D.

Richard F. Haglund Jr., Ph.D.

Yaqiong Xu, Ph.D.

Kirill Bolotin, Ph.D.

Acknowledgements

My PhD dissertation cannot be completed without the support from many people.

First, I would like to express my deepest gratitude to my advisor Professor Jason Valentine for his guidance throughout the past years. He showed me how to think critically and creatively, and he is always patient in listening and offers the most insightful and constructive suggestions. With his valuable suggestions, I not only gained skills in dealing with the challenges and difficulties, but also developed a mindset for research, which will continue to benefit me in the future.

I am deeply grateful to my collaborator Prof. Kirill Bolotin for his generous support on my projects regarding two-dimensional materials. His insightful ideas and inspiring discussions were important for the success of my research.

I would also like to thank my committee members Prof. Kirill Bolotin, Prof. Sharon Weiss, Prof. Yaqiong Xu and Prof. Richard Haglund for their time, support, and suggestions regarding my work.

I would like to give many thanks to my labmates in the Valentine group. Thank you for all the thoughtful discussions and the happy hours that we shared. I really enjoyed the moments with you at laser tag and Bushwackers. Special thanks to Parikshit Moitra for his accompany from the first day I entered this lab. Also special thanks to Yuanmu Yang who is always there for me and has encouraged and helped me through difficulties.

I would also like to thank the group members in the Bolotin group. Thanks to Andrey Klots for discussions and assistances in electrical measurements. Thanks to Dhiraj Prasai for providing me high quality graphene and MoS_2 samples for my experiments.

Most of the device fabrication was done at the Vanderbilt Institute of Nanotechnology and Science (VINSE), and I deeply appreciate Prof. Anthony Hmelo, Bo Choi, and Ben Schmidt for their training and assistance, without which my dissertation would not be possible.

Finally, I wish to thank my family, especially my mother and father. This thesis would have not been possible without their unconditional love. Thank you for your support, your encouragement and your patience waiting for me to graduate.

List of Figures

List of Abbreviations

2D material	Two-dimensional Materials
CMOS	Complementary Metal-oxide Semiconductor
CVD	Chemical Vapor Deposition
DBR	Distributed Bragg Reflector
EBL	Electron Beam Lithography
EIT	Electromagnetically Induced Transparency
ENZ	Epsilon-near-zero
EQE	External Quantum Efficiency
FET	Field-effect Transistor
FRPC	Fano-resonant Photonic Crystal
FWHM	Full Width Half Maximum
Gr	Graphene
ITO	Indium Tin Oxide
LED	Light-emitting diodes
LPCVD	Low-pressure Chemical Vapor Deposition
LSPR	Localized Surface Plasmon Resonance
MoS_2	Molybdenum Disulfide
NEP	Noise Equivalent Power
NIR	Near Infrared
PC	Photonic Crystal
PDMS	Poly(dimethylsiloxane)

PEO	Poly(ethylene oxide)
PMMA	Poly(methyl methacrylate)
PTE	Photothermoelectric Effect
PVE	Photovoltaic Effect
Q-factor	Quality Factor
RIE	Reactive-ion Etching
SCS	Scattering Cross-Ssection
SEM	Scanning Electron Microscope
SPP	Surface Plasma Polariton
TCO	Transparent Conductive Oxide
TE	Transverse Electric
TM	Transverse Magnetic
TMDC	Transition Metal Dichalcogenide
VCSEL	Vertical-cavity Surface-emitting Lasers
VINSE	Vanderbilt Institute of Nanoscale Science and Engineering

List of Publications

Portions of this dissertation have been drawn from the following publications and manuscripts:

1. **W. Wang,** I. Kravchenko, J. Valentine, "Dynamic Modulation of ITO-Huygens' Dielectric Metasurface", Manuscript in preparation.
2. **W. Wang**, A. Klots, D. Prasai, Y. Yang, K. I. Bolotin, J. Valentine, "Hot Electron-Based Near-Infrared Photodetection Using Bilayer MoS2", **Nano Letters** 15, 7440 (2015).
3. **W. Wang**, A. Klots, Y. Yang, W. Li, K. Bolotin and J. Valentine, "Enhanced absorption and photodetection in 2D materials via Fano resonant photonic crystals", **Applied Physics Letters,** 106, 181104 (2015).

Other publications that are related but not directly covered by this dissertation:

4. Y. Yang, **W. Wang**, A. Boulesbaa, I. Kravchenko, D. Briggs, A. Puretzky, D. Geohegan, J. Valentine, "Nonlinear Fano-Resonant Dielectric Metasurfaces", Nano Letters 15, 7388 (2015).
5. W. Li, Z. J. Coppens, L. V. Besteiro, **W. Wang**, A. O. Govorov, J. Valentine, "Circularly polarized light detection with hot electrons in chiral plasmonic metamaterials", Nature Communications, 8379 (2015).
6. Y. Yang, **W. Wang**, P. Moitra, I. Kravchenko, D. Briggs and J. Valentine, "Dielectric meta-reflectarray for broadband polarization conversion and optical vortex generation", Nano Letters 14, 1394 (2014).

Chapter 1

Introduction

1.1 Enhancing Light-matter Interactions in Nanoscale Materials

When light meets matter, an interaction takes place and the manifestation of the interaction, such as reflection, absorption or emission, is determined by both the properties of the matter as well as the light. The interaction between light and nanoscale materials is of particular interest due to its importance in the energy conversion processes where light is converted into other energy forms such as electrical energy, thermal energy, and chemical energy. Since these energy conversion processes typically start with the absorption of photons in the material, their external quantum efficiencies are usually limited by the low absorption in the small volumes associated with nanoscale materials. For an efficient energy conversion device, an enhancement in the light-matter interaction is necessary, and can be achieved by integrating the nanoscale materials with properly engineered optical nanostructures.

1.1.1 Plasmonic Nanostructures: Opportunities and Challenges

Optical nanostructures are structures with dimensions similar or smaller than the wavelength of light. They are capable of supporting optical resonances that induce an electric field enhancement. As such, by combining optical nanostructures with nanoscale materials the material absorption can also be enhanced. At the nanoscale, one of the most general approaches in tailoring and manipulating the electromagnetic field is to utilize the localized surface plasmon resonances (LSPRs) in plasmonic nanostructures.

An LSPR is a surface plasmon polariton (SPP) resonance that is confined in a metallic nanostructure. A surface plasma polariton (SPP) exists in the form of coherent oscillations of electrons at the interface between a metal and a dielectric. It typically has an effective wavelength λ_{spp} much shorter than that of free space light, therefore yielding the possibility of achieving tightly confined light in a subwavelength volume[1]–[4]. The simplest structure to utilize an LSPR is a dipole antenna that supports a Fabry-Perot resonance of the SPP, which results in an enhanced electric field at the two ends of the antenna[4]. The hybridization of two identical antennas could result in either a bright mode with enhanced electric field in the gap[1], or dark modes such as an electric quadrapole that cannot be directly accessed from free space. However, by introducing a third antenna with the orientation perpendicular to the first two antennas, the dark mode can be excited and results in an analogue of electromagnetic induced transparency (EIT), showing high transmission at the central wavelength and exhibiting high electric field strength in the gaps[5]–[7]. Apart from manipulating metallic nano-antennas, a different approach in enhancing light-matter interaction is achieved by creating a metamaterial perfect absorber[8], [9]. In this structure, by overlapping the electric dipole induced by the metal disk and the magnetic dipole formed in the spacing layer between the metal disk and metal back plane, an impedance match between the surface and air can be realized, leading to zero reflection and complete absorption in the structure.

The capability to greatly enhance the electric field and tightly confine light into subwavelength volumes makes SPP resonances appealing for applications such as enhanced light emission, efficient and ultra-thin photovoltaic cells, enhanced non-linear processes, ultra-compact modulators, and photodetectors[10]–[12], as well as

2

subwavelength imaging and lithography[12]–[14]. Some examples include plasmonic lasers based on a metal-insulator-semiconductor (MIS) hybrid waveguides[15], photovoltaic cells in which light is trapped in the active layer due to the scattering from plasmonic nanoparticles[16], significantly enhanced third-harmonic generation in nanoparticles sitting in the gap of a metallic antenna[17], and ultra-compact plasmonic Mach-Zehnder modulators with greatly reduced size compared to other photonic waveguide-based Mach–Zehnder modulators[18].

Despite all the advantages, SPP resonances suffer from ohmic losses due to the scattering of electrons in the metal, which is further amplified by the resonant behavior of the particle. As a result, after excitation, SPPs rapidly decay into energetic hot electrons, and eventually dissipate their energy through thermalization. This parasitic power loss in metal leads to a non-negligible non-radiative decay channel that results in the degradation of efficiency as well as the generation of heat.

1.1.2 Exploiting Plasmonic Loss via Charge Transfer

In order to make use of plasmonic losses, researchers discovered that the hot carriers generated from the non-radiative decay process can be harnessed before their thermalization. Hot electron injection induced chemical reactions such as the splitting of water[19] and the photodissociation of H_2[20], as well as phase transitions in VO_2[21] and monolayer MoS_2[22] have been realized. Recently, the extraction of hot electrons in generating photocurrent has also been demonstrated[23]–[25].
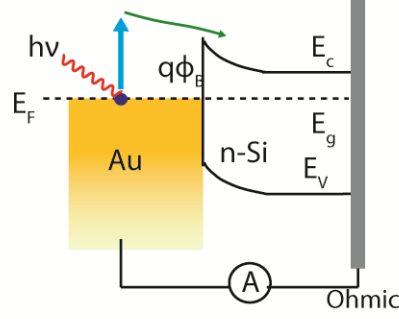
Figure 1.1. Band diagram of a hot electron photodetector. A hot electron crosses over the Schottky interface between a semiconductor and metal, followed by the injection into the semiconductor and the collection at the ohmic contact.

The extraction of hot electrons into useful photocurrent involves the injection of the electrons from a resonant metallic nanostructure into an adjacent semiconductor. The injection is typically achieved using a Schottky barrier between the metal and the semiconductor interface to prevent the backflow of the injected electrons. As is shown in Figure 1.1, a portion of the energetic electrons with energies greater than that of the height of the Shottky barrier $q\phi_B$ can cross over the barrier and get injected into the semiconductor. The injection efficiency η is determined by the Fowler's formula[26], which is expressed by

$$\eta \approx A \times C_f \frac{(h\nu - q\phi_B)^2}{h\nu} \tag{1.1}$$

here A is the absorption in the plasmonic structures, $h\nu$ is the energy of the incident photon and C_f is a device-specific Fowler emission coefficient, which depends on the dimension and shape of the resonant metal particle.

Primarily limited by the short diffusion length in gold and the requirement of the momentum conservation, plasmon-induced hot electron injection efficiency is typically very low. The first demonstrated plasmon-induced hot electron photodetector in the near

4

infrared range had an injection efficiency on the order of 10^{-4} [27]. To address this issue, numerous approaches have been adopted to increase the hot electron injection efficiency, including introducing surface roughness at the metal/semiconductor interfaces to relax the momentum conservation requirement[28], [29], using thin metal films with thickness lower than the hot electron diffusion length, and utilizing metamaterial perfect absorbers[30].

The technique of hot electron injection not only serves as an approach to harness the power dissipated in plasmonic structures, but also provides an indirect channel for the light to interact with matter via the introduction of an intermediate system. Specifically, photons with energy lower than the bandgap of the semiconductor can be converted into hot electrons through plasmon resonances and via the injection process they will eventually end up as free electrons in the conduction band of the semiconductor. In addition, the plasmon resonances in metal nanostructures offer additional advantages in terms of broad spectral tunability and large absorption cross section, making the technique of hot electron injection an excellent candidate in future energy harvesting applications.

1.1.3 Low loss Dielectric cavities and resonators

An alternative approach to circumvent plasmonic losses is to use micro or nanoscale cavities or resonators constructed from dielectric components. Distinct from plasmonic structures, the confinement of electromagnetic fields in dielectric cavities is usually achieved based on the refractive index contrast between high-index and low-index materials. At telecommunication wavelengths (~1.5 μm), silicon with a refractive index about 3.5 is the most common high-index material due to its low intrinsic material

loss, moderate material dispersion, and compatibility with standard semiconductor fabrication techniques.

The quantity to characterize the quality of a cavity is its quality factor (Q factor), which is defined as

$$Q = 2\pi \frac{\text{Energy stored}}{\text{Energy dissipated per cycle}} \qquad (1.2)$$

and can be easily approximated with $Q = \omega_0 / \Delta\omega$, where ω_0 is the resonant frequency of the cavity and $\Delta\omega$ is the spectra linewidth of the resonance. In most applications aimed at increasing light-matter interaction, dielectric cavities with high Q-factors are desired for the strong enhancement of the electric field. The widely adopted dielectric cavity configurations include ring resonators, Bragg cavities, as well as photonic crystal defect cavities. Ring resonators have been used in index sensing and high-contrast modulation[31], [32]; the Bragg cavities composed of two distributed Bragg reflectors (DBRs) are important components in vertical-cavity surface-emitting lasers (VCSEL)[33] and photonic crystal defect cavities have been demonstrated to have excellent potential in enhancing the light emission and non-linear optical processes[34]–[36]. Besides these conventional approaches, dielectric metasurfaces with strongly enhanced electric fields and high quality factors have also been realized, leading to enhanced nonlinear processes in silicon[37].

1.2 Optoelectronic Properties of Ultrathin Films

Integrating semiconductors or other materials with plasmonic or photonic nanostructures can greatly enhance the efficiency of light-matter interaction processes, leading to remarkable performance improvements in optoelectronic devices. However,

6

conventional optoelectronic devices also suffer from issues related to the material selection. For instance, despite its CMOS compatibility, the indirect bandgap of silicon prevents the direct generation of photons, prohibiting its use as a light source. III-V semiconductors such as gallium, indium, arsenide and their compounds are suitable for achieving light emission, however, the stringent requirements of lattice matching make them incompatible with the silicon-based CMOS platform. Ultrathin films such as two-dimensional materials and transparent conductive oxides provide alternative material systems that avoid these issues and are potentially suitable for future high performance light emitters, modulators and photodetectors.

1.2.1   Two-dimensional (2D) Materials

Two-dimensional (2D) materials consist of two dimensional crystal structures that can exist in a free standing form[38], [39]. Following the successful isolation of monolayer graphene from bulk graphite in 2004, the field of 2D materials has experienced fast growth and has attracted intense interest in the investigation of their fundamental properties and applications.

Being composed of a monolayer of carbon atoms arranged in a honeycomb lattice, graphene consists of massless and ballistic electrons[40], which lead to graphene's ultrahigh mobility that has been reported to be over 200,000 cm^2/Vs[41]. An important aspect about graphene is its electronic band structure, which shows a linear dispersion with touching conduction and valance bands at the K and K' point, also known as the "Dirac point"[42]. Interband transitions occur when an incident photon possesses energy higher than twice the Fermi energy ($h\nu \geq 2|E_F|$), where h is the plank constant, ν is the light frequency and E_F is the Fermi energy of graphene. Therefore, when at the

charge-neutrality point where $E_F = 0$, graphene absorbs light within a broadband spectrum with a constant absorbance of $\pi\alpha \approx 2.3\%$ [43]–[45], where α is the fine structure constant. Meanwhile, due to the very low electronic density of states in graphene, the carrier concentration in graphene can be easily controlled via electrostatically gating, which results in a readily tunable Fermi level and thus a controllable interband transition process. Beyond the spectral range of interband transitions, plasmons exist in graphene in the mid-infrared range, providing strong light-matter interaction in the long-wavelength range[46], [47].

Following the rise of graphene, a new family of 2D materials, which can be exfoliated from bulk transition metal dichalcogenides (TMDCs) has emerged in recent years and have been demonstrated as excellent candidates in electronics and optoelectronics applications. In contrast to semi-metallic graphene, TMDCs are two-dimensional semiconductors with bandgaps ranging from 1 eV to 2 eV[48]. Monolayer molybdenum disulfide (MoS$_2$), as a prototypical TMDC, has a direct bandgap at 1.8 eV[48]–[50], making it suitable for light absorption and emission[51], [52]. Moreover, the direct bandgap of monolayer MoS$_2$ is tunable with applied electrostatic gating and strain[55] [56] and can evolve into an indirect bandgap when the number of layers is increased[55], providing additional flexibility in applying it in optoelectronic devices.

In addition to graphene and TMDCs, other 2D materials such as hexagonal boron nitride (hBN) and black phosphorus (BP) have also attracted much attention. For instance, the bandgap of hBN is about 6 eV, making it a good insulator, and the bandgap of BP ranges from 0.3 eV to ~2 eV with a decreasing number of layers[48]. Ultimately, 2D materials offer spectral coverage over a large range of the electromagnetic spectrum.

1.2.2   Transparent Conductive Oxide Nano-films

Another material system that exhibits unique optoelectronic properties is the family of transparent conductive oxides (TCOs) such as indium tin oxide (ITO), aluminum doped zinc oxide (AZO) and gallium doped zinc oxide (GZO). ITO, in particular, is the most widely adopted TCO for applications such as displays, touch panels and solar cells due to its simultaneously large electrical conductivity and optical transparency. It's a highly doped n-type semiconductor with the carriers being contributed by substitutional tin dopants and oxygen vacancies[56]. As such, high carrier concentration, on the order of 10^{20}/cm^3, can be achieved, which leads to a plasma frequency that lies in the near infrared range and allows the use of its plasmon resonances in the telecommunication band. This unique feature distinguishes ITO from graphene as well as the heavily doped semiconductors like silicon, both of which have plasmon resonances only in the mid-infrared and terahertz range.

The carriers in ITO are primarily created during the deposition and their concentration can easily be tuned via controlling the gas content, flow rate, the pressure and the temperature[56], [57], resulting in the modification of the plasma frequency. Similar to graphene, the carrier concentration in ITO can also be controlled via electrostatically gating in a field-effect transistor configuration, and the plasma wavelength of ITO can be tuned from ~3μm to ~0.5μm when the carrier concentration is modified from 10^{20}/cm^3 to 5×10^{21}/cm^3[58] However, the thickness of the carrier depletion/accumulation layer is typically very low[59], as such, an ultrathin film is desired to minimize the damping in the un-switched portion of ITO.

1.3 Application of Ultrathin Films in Optoelectronics

Based on the rich optoelectronic properties of ultrathin films, various devices utilizing such films have been realized, often with performance advantages compared to bulk semiconductors or devices. Applications include but are not limited to broadband and high-speed photodetectors, high-efficiency modulators and highly tunable emitters.

1.3.1   Photodetectors

Owing to its cone-like band structure with zero bandgap, graphene offers opportunities to achieve ultra-broadband photodetection[60]–[63], with the capability of *in-situ* tuning the photoresponsivity via electrostatically gating. Furthermore, the photo-response in graphene is ultrafast. A graphene photodetector with a bandwidth of 40 GHz have been experimentally demonstrated[64], while its intrinsic bandwidth is limited only by the lifetime of the photogenerated carriers and was measured to be 262 GHz[65]. Compared to other high-speed detectors based on III-V semiconductors, graphene photodetectors are CMOS compatible and thus a potentially better candidate for use in high-speed optical communications on silicon chips.

Despite the advantages, efficiencies of the graphene photodetectors that are based on the photovoltaic effect (PVE) are typically low[66]. Photo-generated carriers in graphene have a much shorter lifetime than those in a bulk semiconductor due to the lack of a bandgap. As such, at a graphene/metal junction, only carriers generated within ~0.2 μm of the electrode can be collected by the built-in potential at the contact[67]. Although interdigitated wires composed of different metals have been used for the collection of photocurrent at zero bias[68], the complexity in fabrication as well as the relatively low external quantum efficiency (6.1mA/W) limits use in practical applications.

10

In contrast to graphene, transition metal dichalcogenides (TMDCs) are two-dimensional semiconductors. MoS_2, in particular, is attracting tremendous interest due to its direct bandgap at 1.8 eV with a moderate electron mobility of about $200\,cm^2\,V^{-1}\,s^{-1}$[69]. For light harvesting, MoS_2-based photodetectors have been demonstrated to have the ability to achieve photogain. Due to the trap states near the Shottky junction formed between MoS_2 and the electrodes, the photogenerated holes can be trapped at the junction while the electrons keep circulating in the circuit until the trapped holes are released and recombine with the electrons, as is schematically shown in Figure 1.2. This process is capable of generating photo-amplification with the photogain determined by the trapping time of holes and the drift velocity of electrons. The highest photoresponsivity reported to date is 880A/W, with the noise equivalent power (NEP) lower than that of commercial state of the art silicon p-n junction based avalanche photodiodes[70], [71].
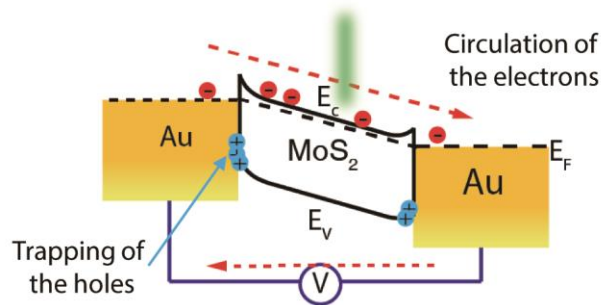
Figure 1.2. Electronic band structure of a visible MoS_2 photodetector in which photoamplification is achieved by trapping the photo-generated holes at the Schottky interfaces.

Enabled by the fact that the individual layers of 2D materials are only weakly bonded through van der Waals forces, various heterostructures exploiting different types of 2D materials have been realized regardless of the restrictions on lattice matching[48]. Consequently, various heterostructures have been demonstrated that take advantage of

11

the properties from different materials, leading to high-efficiency photodetectors and multifunctional electronic logic and memory devices[72]–[74].

1.3.2 Active Modulators

As the propagation of light is essentially based on the interaction between light and matter, it implies that the flow of light can be manipulated by controlling the optical properties of the interacting medium via electrical, thermal[75], mechanical[76] or optical[77] approaches. Among these methods, the electrical modulation of light is of critical importance due to the ability to achieve a fast response from a compact platform that is compatible with silicon technology. The mechanism of electro-optical modulation of ultrathin films, in general, lies in the tuning of the charge concentration or the modification of the electron states.

The modulation of the carrier concentration is usually achieved via electrostatically gating using a field-effect transistor configuration. Graphene is a good example as its Fermi level can be easily adjusted with moderate gate voltage, which has enabled numerous graphene-based modulators with broad bandwidth and fast response[78], [79]. The modulation of ITO is based on a similar mechanism[80]–[82]. The relatively large thickness of ITO thin films compared to that of 2D materials is capable of supporting optical resonant modes inside the film, which can be utilized to enhance light-matter interaction in combination with the resonant modes supported in an optical nanostructure, as will be introduced in Chapter 3.

1.3.3 Light Emitters

Compared to conventional light emitters, emitters based on the 2D materials are exciting mainly due to their highly tunable electronic band structures. For instance, the

direct bandgap of monolayer MoS_2 as well as the interlayer exciton transition between monolayer MoS_2/WS_2 vertical heterojunctions can be easily tuned via electrostatic gating[83], [84]. Moreover, the coverage of photon energy emitted from TMDCs and their heterostructures ranges from visible to the near infrared, making them potentially very useful for the next generation tunable visible light emission devices.

1.4 Motivation and Organization of the Thesis

High-performance optoelectronic devices demand efficient light-matter interaction. Light-matter interaction in ultrathin films, especially 2D materials, can be intrinsically very strong, for instance, the absorption in monolayer graphene, which is only 0.3nm thick, is 2.3%, and the absorption in 0.67 nm thick monolayer MoS_2 is as high as 10% at the excitonic peak. However, their external quantum efficiencies (EQE) are typically limited due to two factors. First, the volume of the interaction is limited by the physical thickness of the thin films, and second, their response to an electromagnetic wave can be anisotropic. Graphene is only one-atom thick and electrons are only movable in-plane, therefore only respond to light with its electric field parallel to the surface. MoS_2 also has anisotropic dielectric constants between the in-plane and out-of-plane directions[85], [86]. The practical application of these ultrathin films requires proper integration with optical nanostructures that are specifically designed according to the different material properties.

In this thesis, I will present my efforts to modify the interaction between light and ultrathin films such as 2D materials and ITO nano-films using different approaches. The enhancement of the interaction in the thin films directly results in the improvement of optoelectronic device performance, which could ultimately lead to applications including

photodetectors and active light modulators.

In **Chapter 2**, I demonstrate that the absorption in 2D materials can be significantly enhanced by incorporating them into a Fano-resonant photonic crystal (FRPC). Both graphene and MoS_2 are implemented with the FRPC structure, and near-unity overall device absorption is demonstrated. More importantly, using photocurrent measurements, I show that 77% absorption in a monolayer graphene can be experimentally achieved, which is over 33 times higher than an otherwise unmodified monolayer graphene film..

Chapter 3 details my efforts to enhance the interaction of light with thin ITO films by combining an epsilon-near-zero (ENZ) mode with a dielectric Huygens' metasurface that is capable of producing electric field enhancements while maintaining near unity transmission. The strongly enhanced electric field together with the absence of material absorption in the silicon resonators results in a transmission modulation of 45%. Preliminary experimental results are presented and explained with simulations.

Chapter 4 introduces a hot electron-based sub-bandgap photodetector using bilayer MoS_2. The spectrum of the photoresponsivity is presented and interpreted with the theory of hot electron injection. A photoamplification that yields a photogain of 10^5 is also demonstrated. The large photogain results in a photoresponsivity of 5.2 A/W, which is far above similar silicon-based hot electron photodetectors in which no photoamplification is present. In addition, control experiments are presented that confirm that the hot electron injection from the plasmon resonances is indeed the source of the photocurrent.

Finally, in **Chapter 5** I give a summary of my work as well as the long term

implications. I will also provide a perspective regarding potential future research directions in which the unique properties of ultrathin films can be combined with optical nanostructures for next generation optoelectronic devices.

Chapter 2

Enhanced Absorption in 2D materials using a Fano-resonant Photonic Crystal

2.1   Introduction

As was mentioned in chapter 1, due to the relatively short interaction length with light and the relatively small single-pass absorption in 2D materials, the performance of 2D material-based optoelectronic devices such as photodetectors and modulators are typically limited. In an effort to enhance the absorption in 2D materials and particularly in graphene, several approaches have been reported. Surface plasmon resonances, despite the fact that they could lead to very high field enhancement, are not the optimal choice due to the relatively high loss in metal. For instance, when graphene is integrated with plasmonic resonators, the absorption in graphene is only enhanced by about 20 times[87], while the rest of the energy is dissipated in the metal. Dielectric resonators, on the other hand, provide an alternative approach to solve this issue. For instance, by integrating graphene with Bragg cavities, the absorption in a monolayer graphene has been enhanced to up to 60%[88].

Here, we report that the absorption in 2D materials can be significantly enhanced by incorporating them into a Fano-resonant photonic crystal (FRPC). We implement the FRPC with both graphene and MoS_2, demonstrating near-unity overall device absorption. More importantly, using photocurrent measurements, we demonstrate that graphene absorbs 77% of the incident light within the telecommunication bands when integrated in the FPRC. This is the highest graphene absorption reported in the telecommunication band at the time when this work is published, to the best of our knowledge. Moreover, we

experimentally show that the absorption in the FRPC is a non-local effect, namely, light can propagate in the structure to as far as 16 μm from the illumination point before being absorbed. For graphene-based field-effect-transistor photodetectors non-local absorption opens up a new route to increase the external quantum efficiency which suffers from the fact that electrons and holes are only separated within a ~0.2 μm region adjacent to the electrodes[67] in the absence of an external bias or photothermoelectric effects[89].

2.2 Fano-resonant Photonic Crystal
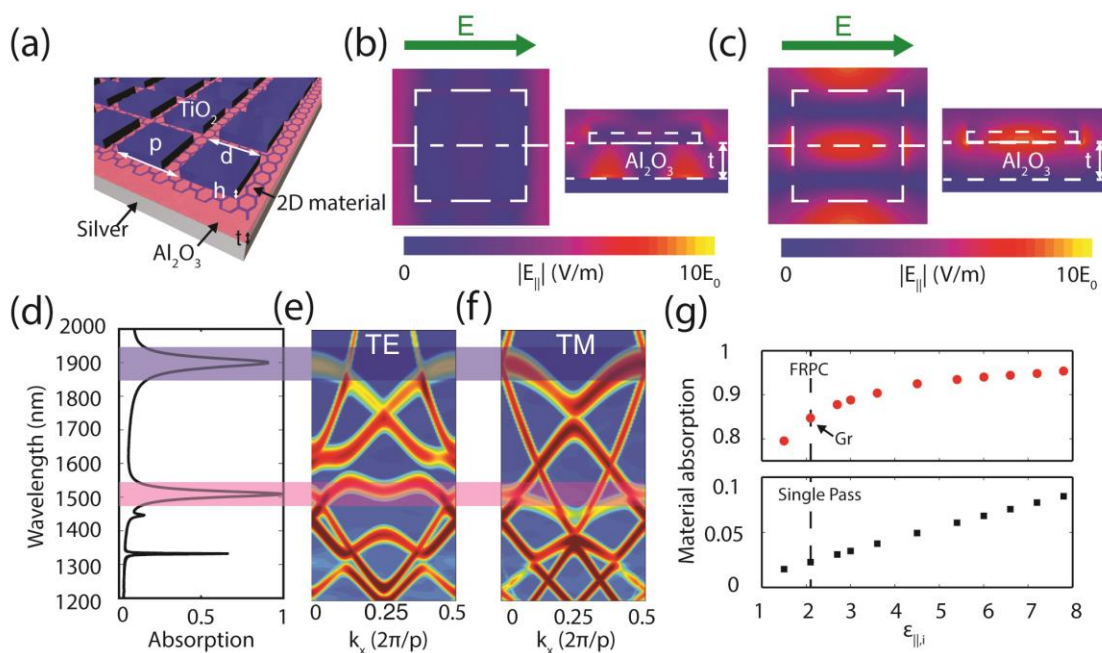
Figure 2.1. (a) Schematic of the Fano-resonant photonic crystal. (b) In-plane electric field components ($/E_{//}/$) of the first band of the Gr-FRPC (near 1900 nm). Left: top view of the $/E_{//}/$ distribution in graphene. Right: cross-section of the $/E_{//}/$ distribution taken along the horizontal dashed line. (c) In-plane electric field components ($/E_{//}/$) of the second band at 1507 nm. (d) Total absorption at normal incidence. (e) Band structure for TE polarization. (f) Band structure for TM polarization (g) Absorption within different 2D materials when integrated with the FRPC structure (upper) and the single pass absorption (lower) as a function of the imaginary part of the in-plane component of the permittivity ($\varepsilon_{//,i}$).

In order to increase absorption, it is essential to achieve modal overlap with the in-plane electric field and the 2D material. We achieve this goal by using the Fano resonance[90] in photonic crystal (PC) slabs. In these Fano resonances, a guided resonance mode excited in the photonic crystal interferes with the free space mode, creating a Fano line shape in the transmission and reflection spectra. Furthermore, we employ a silver back reflector to block transmission, allowing absorption to approach unity. The back reflector is spaced from the PC slab (composed of TiO_2 cubes) by an Al_2O_3 spacer layer and 2D material is sandwiched between the Al_2O_3 and the PC slab, as is shown in Figure 2.1(a). A weak Fabry-Perot cavity is then formed between the silver mirror and the PC slab, providing broadband reflection. Interference occurs between the PC modes and the broadband reflection, resulting in sharp reflection dips. It has been shown previously that in a PC slab the Fano line shape is reduced to a symmetric Lorentzian line shape when direct transmission is zero[91], [92], and reflection at normal incidence is given by[93],

$$R(\omega) = \frac{(\gamma_{rad} - \gamma_{abs})^2 + (\omega - \omega_0)^2}{(\gamma_{rad} + \gamma_{abs})^2 + (\omega - \omega_0)^2} \qquad (2.1)$$

where ω is the frequency, γ_{rad} is the radiative decay rate of the guided resonance mode, and γ_{abs} is the non-radiative decay rate due to absorption. It can be observed that reflection goes to zero at the critical coupling condition when $\gamma_{rad} = \gamma_{abs}$ is satisfied. At the same time, transmission is completely blocked by the silver back plane and as a result absorption approaches unity. The normal-incident total absorption spectrum of a graphene-integrated structure (p =1370 nm, d =950 nm, h =120 nm, t =275 nm) is

shown in Figure 2.1(d). In Figure 2.1(e, f), the band diagrams of the same structure as a function of the in-plane propagation vector k_x are provided. The resonance positions at k_x = 0 match the normal-incident absorption peaks in Figure 2.1(d) and the bands at $k_x > 0$ provide information about the FRPC's angular response. Note that some of the bands in Figure 2.1(e) and 2.1(f) are absent in the absorption spectrum due to the fact that those modes possess different symmetry from modes in air, thus they cannot be coupled to the FRPC from free space. The second band in Figure 2.1(d) at 1507 nm is of particular interest due to the highly confined in-plane E-field occurring at the interface between Al_2O_3 and the PC slab (Figure 2.1c). When graphene, modeled as anisotropic material with no out-of-plane absorption, is present at the interface, it absorbs 79% of the incident light which was calculated by multiplying the material loss with the integration of the E-field within graphene and in the metal, separately. The FRPC performs equally well in the visible regime and for a wide range of 2D materials with varied absorptivity. In Figure 2.1(g) (upper panel), the resonance has been scaled to a wavelength of 540 nm and 2D materials with in-plane imaginary permittivities ($\varepsilon_{//,i}$) ranging from 1.5 to 7.8 are embedded into the FRPC structure. Graphene absorbs 84.7% at the resonance peak while absorption rises up to 95% for materials with larger loss. The single pass absorption of these 2D materials is provided in the lower panel of Figure 2.1(g) for reference.

19

2.3 Enhanced Total Absorption
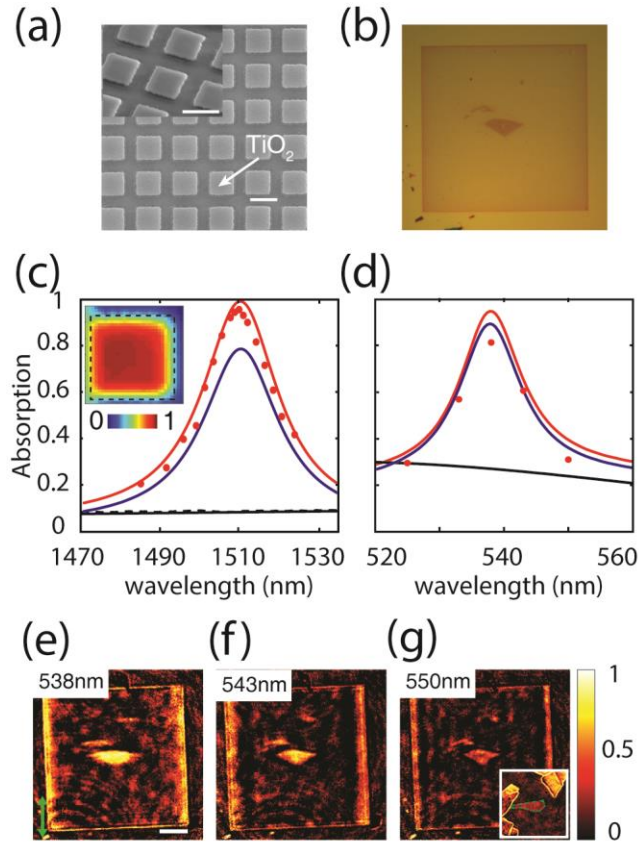
Figure 2.2. (a) SEM of fabricated a FRPC structure designed for graphene, scale bar = 1 μm. (b) Microscope image of the MoS_2-FRPC with a MoS_2 flake at the center. (c) Experimentally measured absorption of the Gr-FRPC (red dots) and absorption of bare graphene on the Al_2O_3/silver stack (black dashed line). The red and blue lines show the simulated total absorption and graphene absorption in the FRPC, respectively. The black line corresponds to the simulated total absorption within the bare graphene. The inset shows the absorption map, the black dashed line indicates the borders of the Gr-FRPC. (d) Total absorption of the MoS_2-FRPC and absorption of MoS_2 in the FRPC (red and blue solid lines). The black line is the absorption of bare MoS_2 on an Al_2O_3/silver substrate. The red dots are the experimentally measured total absorption of the MoS2-FRPC. (e)-(g) Absorption maps of the MoS_2-FRPC array shown in (b) at various wavelengths. The inset of (g) shows the absorption map of bare MoS_2 on an Al_2O_3/silver substrate (the monolayer MoS_2 flake is marked by a green dash line). The green arrow in (e) indicates the incident light polarization and the scale bar is equal to 20 μm.

To experimentally demonstrate the absorption enhancement in 2D materials, we fabricated graphene and MoS_2 integrated FRPC devices (Gr-FRPC and MoS_2-FRPC). Graphene is chosen due to its relatively poor absorption compared to TMDCs, thus

representing the worst-case scenario, while MoS$_2$ is selected as a representative of TMDCs that absorb in visible regime. Monolayer CVD graphene (confirmed by Raman spectroscopy), or monolayer exfoliated MoS$_2$, were transferred onto a Al$_2$O$_3$/silver stack and a TiO$_2$ photonic crystal with an area of 100 μm x 100 μm was defined on top. Images of a fabricated FRPC structure designed for graphene and a MoS$_2$-FRPC device are shown in Figure 2.2(a, b), respectively. In the MoS$_2$-FRPC, the flake is smaller than the array and sits at the center.

From the band structure shown in Figure 2.1(e) and (f), it is obvious that the FRPC mode is sensitive to the angle of incidence. As such, to measure the optical absorption of the Gr-FRPC, the incident angle was confined to within ±2.5° of normal to the substrate. A tunable diode laser with full width half maximum (FWHM) less than 200 kHz (New Focus 6326) was used as the laser source and reflection from the center of the array (R) was measured, yielding the absorption, $A = 1 - R$. A peak absorption of 96% was obtained at 1507 nm and matches well with the simulation (Figure 2.2c). The absorption of bare graphene sitting on the same Al$_2$O$_3$/silver stack but without the PC was measured to be ~8.5%, also matching the simulation. It is important to note that these measurements include absorption in both graphene and the silver back plane. An absorption map is presented in the inset of Figure 2.2(c), showing uniform near-unity absorption on the FRPC array and absorption drops away at the edge of the array.

For the MoS$_2$-FRPC, the resonance is designed to be at 538 nm (p =387 nm, d =172.2 nm, h =46 nm, t =203.5 nm). In this case, 16 nm of PMMA was spun on top of the device to match the resonance wavelength with the laser. The solid red and blue curves in Figure 2.2(d) are the simulated total FRPC absorption and absorption within

21

MoS$_2$ as a function of wavelength, showing values of 95% and 90% at the resonance peaks, respectively. This is higher than in the case of graphene as MoS$_2$ is more absorptive in this wavelength region. For reference, bare MoS$_2$ on top of the Al$_2$O$_3$/silver substrate has ~25% absorption across the wavelength range of interest. The fact that the small piece of MoS$_2$ is embedded in the FRPC array allows us to directly visualize the absorption enhancement in MoS$_2$ by illuminating the entire array with a collimated laser at various wavelengths, both on and off resonance. A map of absorption is obtained by comparing the reflectance intensity obtained from the MoS$_2$-FRPC and from a mirror, as is shown in Figure 2.2(e) (on resonance), and (f, g) (off resonance). The absorption values from the center of FRPC array where MoS$_2$ is present were extracted and are plotted with red dots in Figure 2.2(d). The illumination laser has a FWHM of 3-4 nm and the measured absorption is the average value within this bandwidth, lowering the measured value compared to the simulation. For comparison, the inset of Figure 2.2(g) shows a map of bare MoS$_2$ on top of Al$_2$O$_3$/silver illuminated at 538nm with a measured absorption of 24.6%, closely matching the simulation.

2.4   Enhanced Absorption in 2D materials

While the total absorption enhancement in the Gr-FRPC and MoS$_2$-FRPC clearly indicate strong light-matter interaction, these measurements do not allow us to experimentally validate the percentage of absorption in the 2D materials. To extract this information, we measured the photocurrent from a Gr-FRPC device and compared the result with the photocurrent from bare graphene sitting on top of the same Al$_2$O$_3$/silver stack.

The fabrication of the device (Figure 2.3 a-d) started with silver being deposited onto a p-type silicon wafer which was cleaned with HF, followed by deposition of 40 nm of Al_2O_3 using electron beam deposition. This thin layer of Al_2O_3 protected the silver film during the following step in which 235 nm of Al_2O_3 was grown using atomic layer deposition (ALD). CVD grown graphene was then transferred on to the silver/Al_2O_3 stack. The photonic crystal array was then defined by electron beam lithography (EBL) followed by electron beam deposition and lift-off of the TiO_2 resonator layer. Electrodes were then defined using EBL patterning and deposition of 25 nm Ti and 25 nm Au layers on top of the graphene sheet. The distance between the two electrodes was 180 μm and the width of the electrodes was 210 μm. Thick Cr/Au electrode pads were then defined using EBL for wire bonding. Lastly, graphene was patterned using EBL and O_2 plasma etching to form a patch ~300×400 μm in size.
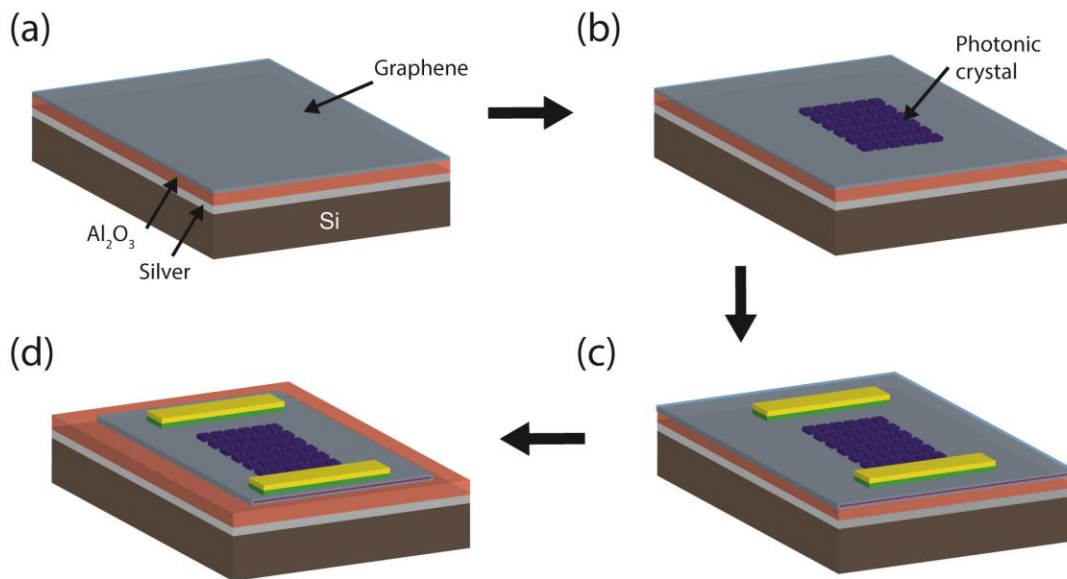
Figure 2.3. (a) Prepare the silver/Al_2O_3 and transfer graphene onto the stack. (b) Define the TiO_2 photonic crystal. (c) Define the electrodes, including the contact electrodes and the thick wire bond pads (not shown). (d) Pattern graphene into a square patch.

The schematic of the photodetector device is shown in Figure 2.4(a), a source drain bias of V_{sd} = -4.1V was applied over a 180 μm long channel with a channel width of 210 μm to negate the variations in the Fermi level due to doping non-uniformities that resulted from the fabrication process. Note that the DC current was measured to be I_{DC} ~ 1.1 mA, resulting in an electrical power density of ~12 W/cm^2, which is small enough to avoid significant Joule heating of the film[94]. A gate voltage V_G = 60V was used to ensure that the Pauli blocking is not active[95]. The device was illuminated in the middle of the Gr-FRPC array and a reference measurement was taken on bare graphene (points A and B in Figure 2.4a). The incident laser beam, with a spot size greater than 15 μm and the E-field polarized parallel to the electrodes, was located 50 μm away from the nearest electrode. The illumination power was kept low so that the power absorbed by graphene is less than 35 μW. With this setup, the measured photocurrent is a result from photovoltaic and bolometric effects[96], both of which increase by the same amount due to the enhanced absorption. The current from the thermoelectrical effect[89], [97], [98] is negligible due to the fact that this effect is based on the difference in the Seebeck coefficient between two different regions, which is negligible under the applied source-drain voltage.

The experimentally measured photocurrent from the device, $I_{FR}(\lambda)$, and from bare graphene, $I_{Gr}(\lambda)$, are shown in Figure 2.4(b), with the peak current occurring at 1507 nm, matching well with the shape of the simulated graphene absorption in FRPC. Comparison of $I_{FR}(\lambda)$ to the mean value of $I_{Gr}(\lambda)$ yields an experimental photocurrent enhancement of 14.33 at the center of the resonance (Figure 2.4c). As a reference, the

theoretical absorption within graphene for the case of a bare film sitting on the same Al$_2$O$_3$/silver stack is 5.23% at 1510 nm with an average value from 1480 nm to 1530 nm of 5.4% (solid line in the inset of Figure 2.4b), yielding a theoretical absorption enhancement of 14.63. The measured photocurrent enhancement is thus close to the simulated absorption enhancement and indicates that 77% of the light is being absorbed within the graphene layer. The photocurrent as a function of the incident power measured at the center of the Gr-FRPC array is shown in Figure 2.4(d), which is taken under the same electric field polarization and the source-drain bias, showing the linear response regarding to the incident power.
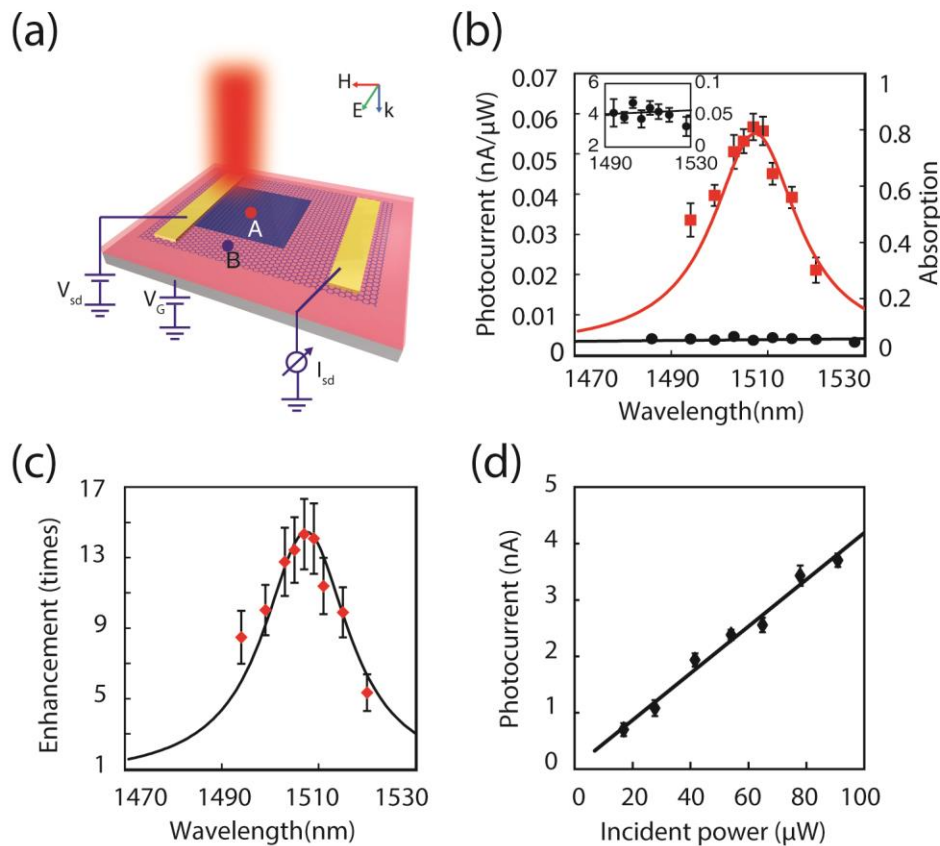
Figure 2.4. (a) Schematic of the Gr-FRPC photodetector device. (b) Photocurrent from the center of the Gr-FRPC array (point A in Figure 2.4a) (red dots) and on bare graphene, corresponding to point B (black dots). The red and black solids lines correspond to the simulated graphene absorption in the FRPC and on an Al$_2$O$_3$/silver substrate, respectively. Inset: zoom in of the graphene photocurrent and simulated graphene absorption for the

case of bare graphene. (c) Experimental enhancement of the photocurrent (dots) and the simulated graphene absorption enhancement (line). (d) Photocurrent from center of Gr-FRPC (point A) as a function of the incident laser power.

2.5   Nonlocal Absorption

One of the key features of our structure is that absorption is non-localized due to propagation within the photonic crystal. Opposed to conventional photonic crystal cavities where light is confined within a small volume, photons in the FRPC are confined vertically to a thin region near the 2D material but are free to propagate in the lateral direction. Figure 2.5(a) shows the intensity of the in-plane electric field ($|E_{||}|^2$) when a Gaussian beam with a $1/e^2$ half-width of $w_{gaus}/2 = 4.5$ µm and E_y polarization is incident on a FRPC that has not been integrated with a 2D material. As can be observed, the field spreads out in the x direction and fitting the envelope of the field intensity along the white dashed line gives a Lorentzian line shape with a half width in the x direction of 28.4 µm, indicating that light propagates ~ 24 µm away from the spot of incidence. The intensity profile along the grey dashed line matches a Gaussian line shape whose half width is 5.6 µm.

To demonstrate non-local absorption experimentally, we scanned a laser beam with a $1/e^2$ half width of 4.5 µm over a FRPC that was partially covered by graphene. The sample was broken down into 3 regions, as shown in Figure 2.5(b), where region I consists of the FRPC, without graphene, region II consists of the FRPC with graphene, and region III is void of the FRPC. Absorption in region I is soley due to ohmic loss in the metal back plane while absorption in region II is dominated by graphene. Due to the finite beam size and propogation within the PC, the measured absorption, as a function of position, is blurred as the beam approaches the border between regions I and II (black

line Figure 2.5b). The electric field distribution in the x direction can be expressed with a normalized Lorentzian function $f(x, x')$, where x' is the center of the Lorentzian as well as the center of incident beam spot. When the laser scans across the region I/II boundary (where $x = x_1$), the measured absorption $A_{scan}(x')$ at position x' is an addition of

$$A_1 \int_{-\infty}^{x_1} f(x, x') dx \text{ and } A_2 (1 - \int_{-\infty}^{x_1} f(x, x') dx),$$ where A_1 and A_2 are the absorption coefficients

in region I and II, respectively. The first term represents the portion of electric field left in region I being multiplied by the absorption coefficient in region I, resulting in the total absorption in region I, and the same second term stands for the total absorption in region II. Taking the derivative of $A_{scan}(x')$, we obtain $\frac{\partial}{\partial x} A_{scan}(x') \propto f(x, x')$ demonstrating that the derivative of absorption, as a function of position, is proportional to the field distribution in FRPC.

The derivative of the measured absorption is shown in Figure 2.5(c) (red line) and the data to the left of the green dashed line is fitted with a Lorentzian curve (red dashed line). To the right of the green dashed line the response of the FRPC is dominated by the unpatterned area (region III) and absorption begins to dip. From the fit to the derivative of absorption, we obtain an intensity distribution whose $1/e^2$ half width within the FRPC is 20.7μm, indicating a propagation distance of ~16 μm from the incident spot. This value is slightly smaller than the calculated value of 24 μm and the error most likely arises from defects within the FRPC due to fabrication imperfections and contamination from the graphene transfer process. It should also be noted that the simulated propagation distance in region II is only 8.9 μm due to the existence of graphene which introduces a larger non-radiative decay rate. This indicates that in our photocurrent enhancement

measurements light is not making it to the electrodes, but rather being absorbed within the FRPC and thus the current enhancement is due to absorption enhancement rather than more effective charge collection.
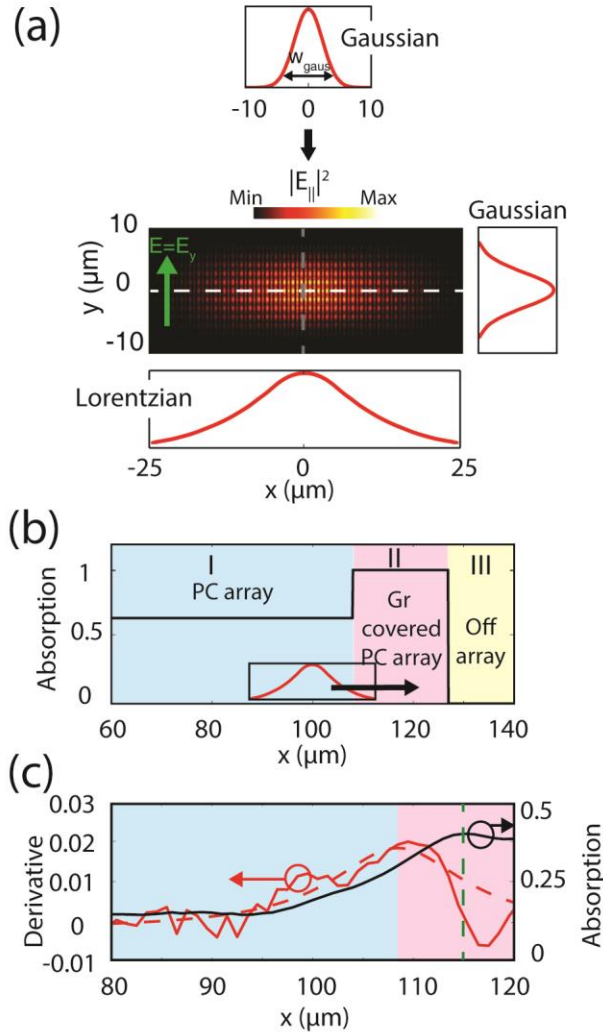
Figure 2.5. (a) Intensity plot of the in-plane electric field ($/E_{///}/^2$) distribution when a Gaussian beam is incident on the FRPC without graphene. Top: $/E/^2$ of the incident beam. The two curves on the bottom and right are envelopes of $/E_{///}/^2$ taken along the white and grey dashed lines within the FRPC. (b) Normal incident absorption profile of the FRPC array partly covered by graphene. The inset depicts the light field within the FRPC and the direction of laser beam movement. (c) Absorption and the derivative of absorption near the region I/II border. Experimentally measured absorption (black line), derivative of the experimentally measured absorption (red line) and the fit to the derivative of the absorption (red dashed line).

Since the FRPC structure is sensitive to the angle of incidence, below we illustrate that the absorption enhancement and the non-local absorption are not coming from other guided modes excited at angled incidence. We examine the absorption in the FRPC without graphene as a function of the incident angle, as can be observed in Figure 2.6. The TM mode is less sensitive to the incident angle compared to the TE mode. The $|E_{///}|$ distribution at multiple angles of incidence for both TE and TM polarization are show in Figure 2.6(c-e). All field plots are taken at the normal incident resonance wavelength indicated by the dashed line in Figure 2.6 (a, b), which is also the wavelength used in the non-local simulations and experiments. The field profiles for the TM mode at incident angles of 3 °and 6 °, shown in Figure 2.6 (d, e), exhibit the same mode profile as normal incidence (Figure 2.6c). For TE polarization, when the angle of incidence is greater than 2 °, absorption becomes less than 12%. The $|E_{///}|$ distribution for TE polarization at 1 °is shown in Figure 2.6 (f) which is also the same as the normal-incident mode. From these results, it is clear that even when illuminated with a Gaussian beam with a finite range of off-normal incident angles, the same mode is excited in the FRPC so that non-localized absorption as well as any absorption enhancements are not coming from other guided modes within the structure.
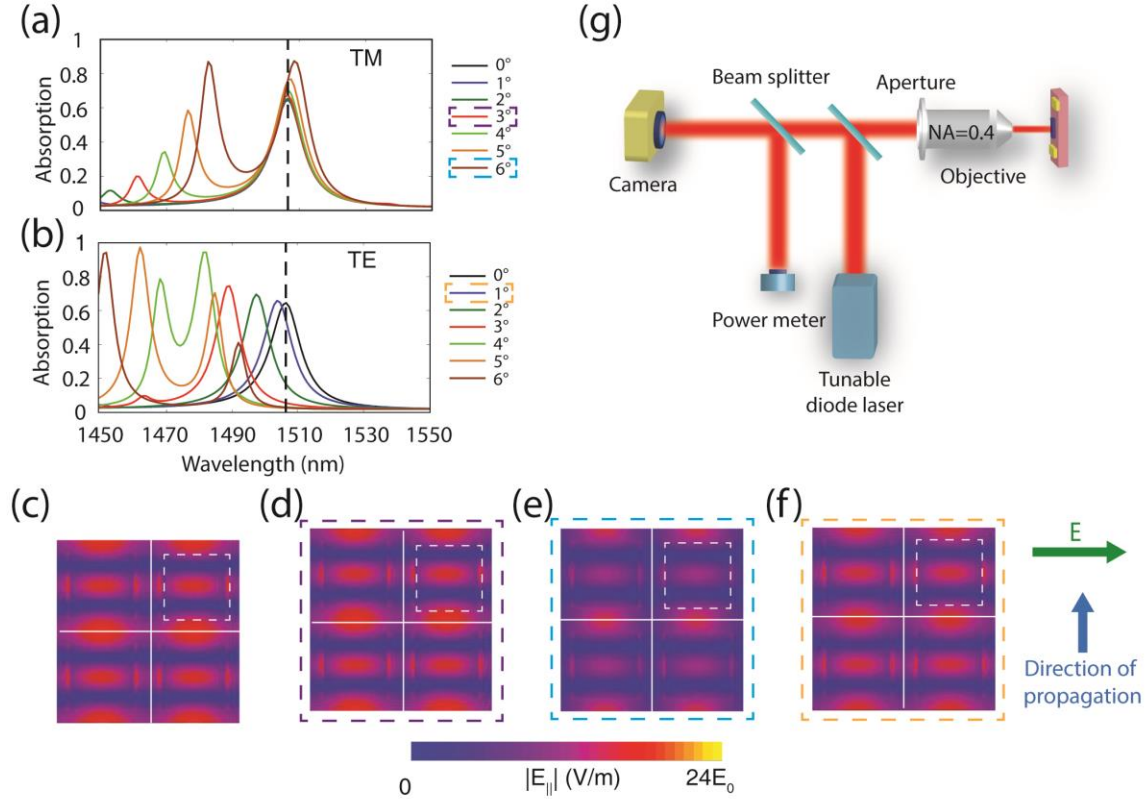
Figure 2.6. Absorption vs. incident angle for (a) TM polarization and (b) TE polarization. (c) $|E_{||}|$ distribution on top of Al_2O_3 with $0\,°$ incidence at the resonance wavelength (dotted lines in (a) and (b)). The plot includes 4 unit cells defined by the white cross and the dashed square indicates the position of the TiO_2 cube within the unit cell. (d) $|E_{||}|$ for TM polarization at $3\,°$ incidence. (e) $|E_{||}|$ for TM polarization at $6\,°$. (f) $|E_{||}|$ for TE polarization at $1\,°$. (g) Measurement setup that confines the incident angle by using the aperture at the back of the objective.

2.6 Conclusion

In summary, we have experimentally demonstrated that optical absorption in 2D materials as thin as a monolayer of graphene can be increased to 77% by integrating the material within Fano-resonant photonic crystals. Furthermore, the same structure is able to enhance absorption in other 2D materials in the visible regime with absorption in the 2D material reaching values of up to 90% in the case of MoS_2. We also demonstrated that the FRPC structure can be utilized to collect photons incident 16 μm away from the 2D material flake thus increasing the effective detection area, which is typically limited by

the flake size. Potential applications rising from this concept include long channel graphene-based FET photodetectors with greatly enhanced external quantum efficiency while still maintaining an ultrafast photoresponse.

Chapter 3

Enhanced Modulation using ENZ-Huygens' Hybrid Mode

3.1 Introduction

The interaction between light and matter not only allows for the detection of photons, but also enables the active modulation of light by controlling the optical properties of the material. A wide variety of material systems have been demonstrated to have controllable optical properties, for instance, phase change materials [99], transparent conductive materials (TCOs)[56], and newly-emerged low-dimensional materials such as graphene[100] and quantum dots[101]. For nanoscale modulators using thin films, the modulation often suffers from limited interaction length which results from the small volume of the material. However, integration of the active materials with optical nanostructures can be used to enhance the light-matter interaction.

Utilizing plasmon resonances is the most common approach in achieving active light modulation with devices usually being implemented using plasmonic "metasurfaces". In addition to providing high enhancement of the local electric field, plasmonic metasurfaces are capable of molding the properties of light, such as the intensity, polarization and spin/orbital angular momentum. The integration of the active materials with such metasurfaces has resulted in the realization of metasurface-based modulators with various functionalities[102]–[105].

However, plasmonic metasurfaces are inherently lossy, leading to inevitable power loss in the metal. Consequently, their performance suffers in terms of the

modulation depth and the insertion loss. Dielectric metasurfaces[106], on the other hand, have proved themselves to be excellent alternatives to their plasmonic counterparts mainly due to the absence of material losses. Here, we demonstrate an efficient light modulator based on a dielectric Huygens' metasurface integrated with an ultrathin ITO film, whose plasma frequency can be dynamically tuned in the near-infrared range through electrostatically gating. We show that this integration enables us to perform modulation in the transmission mode with a low insertion loss. The overlapping of the Huygens' mode with an epsilon-near-zero (ENZ) mode in the ultrathin ITO film results in 45% transmission modulation. Compared to monolayer graphene, ITO is selected for its higher plasma frequency which lies in the near infrared range. Also, the existence of the ENZ mode requires a finite thickness, therefore it cannot be found in monolayer graphene.

3.2 Dielectric Metasurfaces

3.2.1   Mie Resonances

The building block of dielectric metasurfaces are high refractive index resonators exhibiting Mie resonances. Unlike the plasmon resonances in metallic structures, which result from the oscillation of conduction currents on the metallic surface, Mie resonances are electromagnetic resonances in dielectric nanoparticles and can exhibit electric and magnetic dipoles associated with displacement currents. Since the confinement of the electric field inside the nanoparticle is based on the refractive index contrast at the boundaries, high-index materials are always desired.
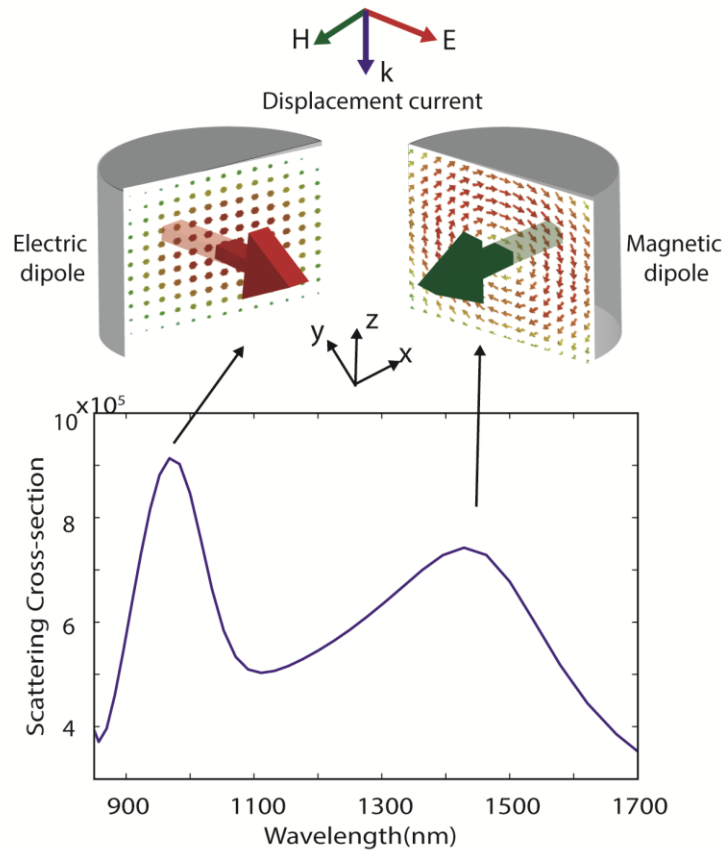
Figure 3.1. The scattering cross-section (SCS) of a silicon nano-cylinder with a diameter of 400 nm and height of 300nm. The field plots show the electric (left, green arrow) and magnetic dipole (right, red arrow) and the corresponding displacement current.

In the near infrared range, due to the relatively high refractive index and the absence of the material loss, silicon is the most commonly used material in realizing Mie resonances. Figure 3.1 shows the scattering-cross section (SCS) of a silicon cylinder with 400 nm diameter and 300 nm height. The displacement current plots clearly show the profile of an electric dipole (left) and a magnetic dipole (right) at the corresponding SCS peaks of 930 nm and 1430 nm, respectively. From the distribution of the displacement current, it can be observed that while the electric dipole is accompanied by an enhancement of the electric field oriented in the x-y plane, the magnetic dipole, which is associated with a circulating displacement current, offers the opportunity to create an electric field enhancement in the z-direction, which is parallel to the incident wave vector.

Therefore, by choosing an appropriate resonance mode, Mie resonances can potentially be utilized in manipulating the orientation of the local electric field.

3.2.2 Huygens' Metasurfaces

In 1690, Huygens pointed out that every point on a wave front acts as a source of outgoing waves[107], which qualitatively explains the propagation of waves in a medium. Two hundred years later, a rigorous form of Huygens' principle was developed, specifying that the "source" should consist of fictitious crossed electric and magnetic dipoles in order to realize pure forward-propagating waves[108]. These fictitious electric and magnetic dipoles have been shown to be realizable using subwavelength structured plasmonic elements that support both electric and magnetic dipolar resonances in the microwave and mid-IR frequencies[109], [110]. However, when moving into the optical frequencies, the power dissipation in plasmon resonances will lead to an undesired decrease in transmission, due to absorption loss.

One way to circumvent absorption loss is to use the dielectric particles as the resonant elements. Dielectric resonators can support overlapped electric and magnetic resonances with minimum parasitic loss[111]. When the resonators are arranged in a subwavelength lattice, the reflectance from the array is described by [111]

$$r = \frac{2i\gamma_e\omega}{\omega_e^2 - \omega^2 - 2i\gamma_e\omega} - \frac{2i\gamma_m\omega}{\omega_m^2 - \omega^2 - 2i\gamma_m\omega} \qquad (3.1)$$

where ω_e and ω_m are the frequencies of the electric and magnetic dipole, γ_e and γ_m are the damping of the two dipoles, respectively. It can therefore be understood that when the electric and magnetic dipoles perfectly overlap with equal strength and damping, the surface will have zero reflection and unity forward-scattering.

3.3 Epsilon-near-zero Modes

In order to actively modulate the transmission of the Huygens' metasurface, we integrate it with an active material such as a thin film of ITO whose electron concentration can be dynamically controlled via electrostatically gating. Moreover, it is desirable that an optical resonance possessing highly enhanced electric field can exist in this deep-subwavelength film. Such electric field enhancement can be achieved when the ITO's permittivity approaches zero.

The ITO can be modelled as a metal with a permittivity expressed by the Drude model, $\varepsilon_{ITO} = 1 - \omega_p^2 / (\omega^2 + i\gamma\omega)$, where ω_p is the plasma frequency and γ is the Drude damping. At the interfaces of a dielectric/ITO/dielectric system shown in Figure 3.2 (a), a solution of the Maxwell equations exists and can be characterized by [112]

$$1 + \frac{\varepsilon_1 k_{z3}}{\varepsilon_3 k_{z1}} = i\tan(k_{z2}d)(\frac{\varepsilon_2 k_{z3}}{\varepsilon_3 k_{z2}} + \frac{\varepsilon_1 k_{z2}}{\varepsilon_2 k_{z1}}) \tag{3.2}$$

where $k_{zi} = \sqrt{\varepsilon_i \frac{\omega^2}{c^2} - k_{\parallel}}$ is the wave vector normal to the interfaces. In particular, the long range SPP branch shows a uniquely flat dispersion near to the position when $\mathrm{Re}(\omega)/\omega_p = 1$ [112]. Since the permittivity of ITO vanishes at this frequency range, this resonant mode is defined as the epsilon-near-zero (ENZ) mode.

Due to the constraints of the boundary condition at the interfaces, which requires the continuity of electric flux density and is expressed as $\varepsilon_1 E_{norm,1} = \varepsilon_2 E_{norm,2} = \varepsilon_3 E_{norm,3}$, the ENZ mode can lead to a highly enhanced electric field in ITO nano-film, as is shown in Figure 3.2(b). Therefore, the utilization of the ENZ mode will result in high modal overlap and therefore strong light-matter interaction within the ITO nano-film.
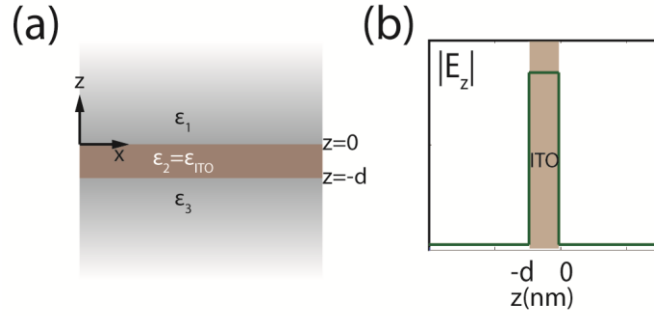
Figure 3.2. (a) Schematic of a three layer system with an ITO nano-film in the middle. (b)The normal component of the electric field is highly enhanced in the nano-film at the ENZ mode.

3.4 Structure Design and Simulation

Our design utilizes the Huygens' metasurface and a dynamically tunable ENZ mode supported in an ultrathin ITO film. Figure 3.3 shows the schematic of the structure, with silicon cylinders supporting both electrical and magnetic resonances and the ultrathin ITO film ($<$ 10 nm) covering on the top. To electrically connect the ITO film on the top, narrow silicon wires were made to run through the cylinders in the y direction.
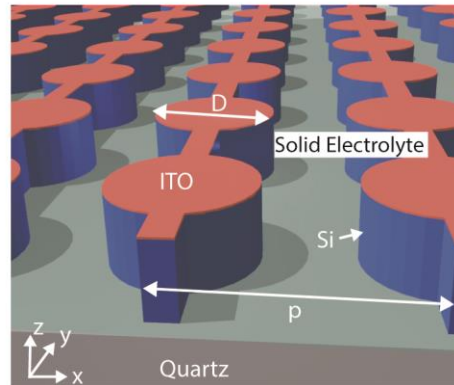
Figure 3.3 Schematic of silicon Huygens' metasurface with ITO thin film on top. The structure is buried in a solid electrolyte film with thickness of 500 nm.

The design of the structure starts with the overlapped electric and magnetic resonances in the silicon cylinders with a height H fixed at 260 nm. To identify the conditions required for the electric and magnetic dipoles to overlap, we simulated the

transmission spectrum with the cylinder diameter D swept from 300 to 700 nm while the period p was kept constant at 820 nm, as is shown in Figure 3.4 (a, b). For the polarization with the electric field along the x direction, the overlapping of the two resonances occurs at $D = 530$nm, resulting in a transmission of 99.5% at 1534 nm and an overall transmission over 90% from 1300 nm to 1800 nm. In contrast, when the two resonances are incompletely overlapped ($D = 400$ nm) or if they are separated ($D = 640$ nm), one or two dips show up in the spectrum. The co-existence of the orthogonal electric and magnetic dipoles at 1534 nm can also be observed from the electric and magnetic field profiles in Figure 3.4 (c). Meanwhile, due to the presence of the magnetic dipole, which is induced by the circulating displacement current in the cylinder, the out-of-plane component of the electric field is enhanced at the top and bottom surfaces of the cylinders, which can be seen in the distribution of $|E_z|$ in Figure 3.4(d). Due to the presence of the wires in the y direction, the transmission spectrum for the E_y polarization does not exactly match with the E_x polarization, although the underlying physics regarding the overlap of the electric and magnetic dipoles is essentially the same. It also needs to be noted that the entire device is embedded in a solid electrolyte film to electrostatically gate the ITO thin film. However, since the refractive index of the solid electrolyte ($n = 1.46$) is comparable to the quartz substrate, and the thickness of the film, which is around 500 nm, is enough to bury the silicon cylinders, the introduction of the film will only slightly shift the Mie resonant spectral positions and will not significantly affect the overlap of the electric and magnetic dipoles. All simulations shown in Figure 3.4 have the 500 nm solid electrolyte film taken into consideration.
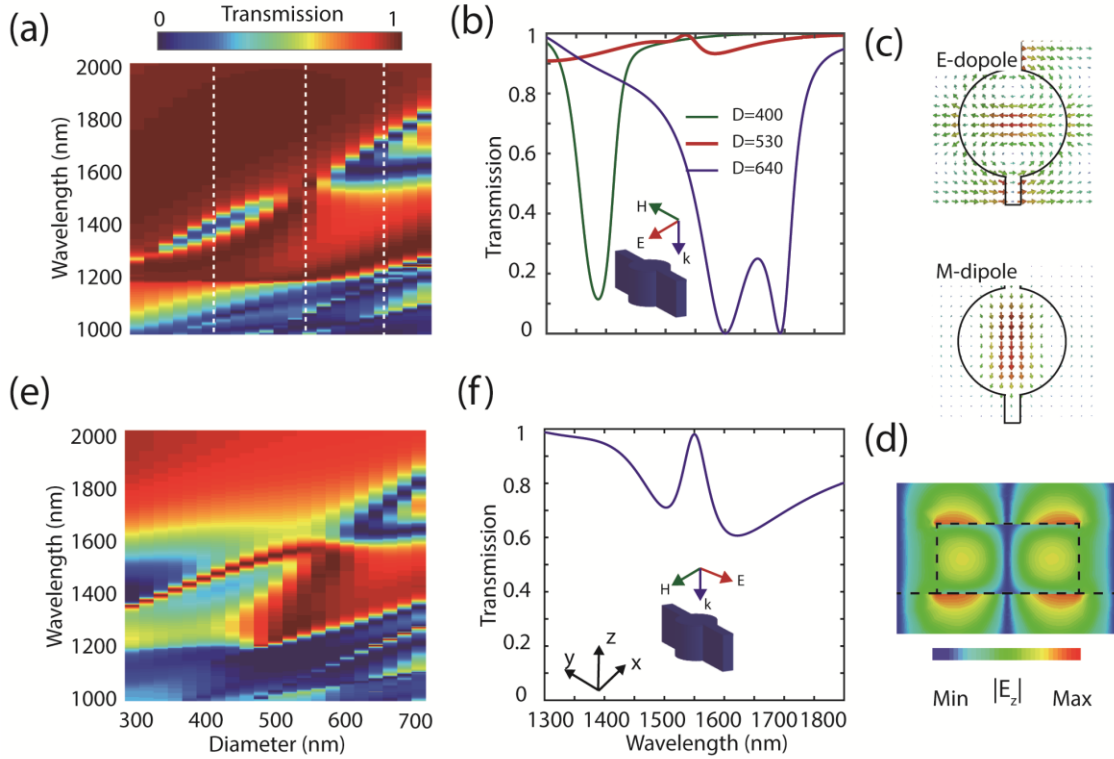
Figure 3.4 (a) Transmission of the silicon cylinder metamaterial as a function of the diameter (D) for E_x polarization (b) Transmission spectrum taken when the diameter is 400 nm, 530 nm and 640 nm, respectively, which correspond to the three white dash lines in (a). (c) Co-existence of the electric and magnetic dipole at 1541nm when $D = 530$ nm. The arrows in the top panel show the electric field and the arrows in the bottom panel show the magnetic field. (d) Distribution of $|E_z|$ at the Huygens' mode for E_x polarization. (e) The transmission map for E_y polarization. (f) The transmission spectrum for E_y polarization when $D = 530$nm.

The next step of the design involves the further overlapping of the Huygens's metasurface with the ENZ mode in ITO. To achieve this, we implement an ITO film with 8.5 nm thickness and λ_p at 1460 nm and integrated it with a Huygens' mode at 1485 nm ($H = 250$ nm, $D = 500$nm, $p = 800$ nm). The thickness of the ITO film is chosen to be thin enough such that efficient carrier depletion or accumulation can be achieved. In the meantime, the film is still continuous and conductive. Both the ENZ mode and the Huygens' mode are capable of inducing E_z field enhancement, therefore the spatial overlap of the two modes in both frequency and polarization leads to a greatly enhanced

E_z field in ITO, with an enhancement factor of 11.5 times compared to the free space electric field strength (E_0), as is shown in the inset of Figure 3.5(a). The absorption in the 8.5 nm thick ITO film thus reaches 46%, which is determined by $\int \varepsilon_i \, | \, E \, |^2 dV$, where ε_i is the imaginary part of the ITO permittivity.

Since the ENZ mode occurs at the frequency where the permittivity of ITO approaches zero, by dynamically tuning the plasma frequency away from the Huygens' mode λ_H, a reduction in the coupling between two modes will result. The decoupling results in a decrease in the electric field within the film resulting in lowering of the absorption within the ITO. The simulated change in absorption as a function of the plasma wavelength λ_P of ITO is presented in Figure 3.5 (a), with the highest absorption occurring at λ_P =1460 nm. The same figure is re-plotted in Figure 3.5(b), but with each absorption curve being shifted by 0.2. It is interesting to note that a hint of anti-crossing occurs when λ_P approaches the wavelength of the Huygens' mode, which implies the existence of strong coupling between the ENZ mode and the Mie resonances of the dielectric metasurface. In general, strong coupling arises when the coupling strength between the two resonances exceeds the average decay rate[113]. In our case, the ENZ mode and the Huygens' mode are able to communicate through the simultaneously enhanced E_z field in the ITO film, followed by efficient energy exchange. However, the anti-crossing is difficult to distinguish due to the strong damping from the absorption in ITO. Strong coupling between the ENZ mode in a doped semiconductor nanolayer and metal split-ring resonators[114] has been previously observed and analyzed, yet this is the first time that the strong coupling between an ENZ mode and a dielectric Mie resonance has been observed.

As a result of the variation in absorption, the transmission of the metasurface is also modulated, as is shown in Figure 3.5 (c, d), 43.2% and 46.5% of modulation in transmission can be expected from E_x and E_y polarization when λ_P is shifted from 1920 nm to 1460 nm. The corresponding tuning of electron concentration is from $4.4 \times 10^{20}/cm^3$ to $7.4 \times 10^{20}/cm^3$.
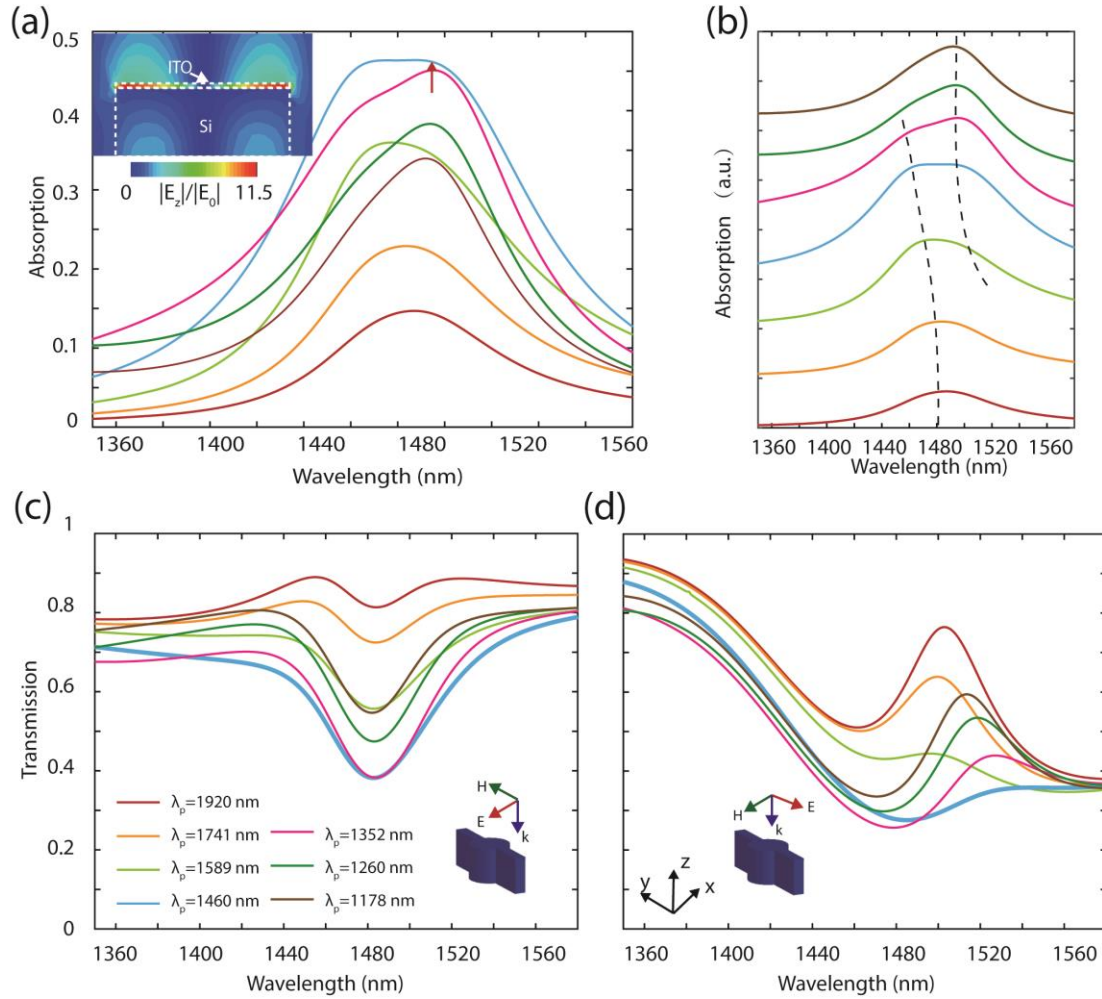
Figure 3.5. (a) Absorption modulation for E_x incidence when the plasma wavelength of ITO is shifted from 1920 nm to 1178 nm. The inset shows the confined electric field $|E_z|$ in the ITO thin film taken at 1480nm (shown with the red arrow). The inset is stretched in the vertical direction by 2 times and only contains the top portion of the silicon resonator so that the ITO layer can be clearly seen. (b) Re-plotted absorption curves in (a) with each curved shifted by 0.2, the black dashed lines are the guide to the eye of the anti-crossing. (c) Transmission modulation for E_x polarization. (d) Transmission modulation for E_x polarization.

41

3.5 Device Fabrication and Dynamic Modulation Experiments
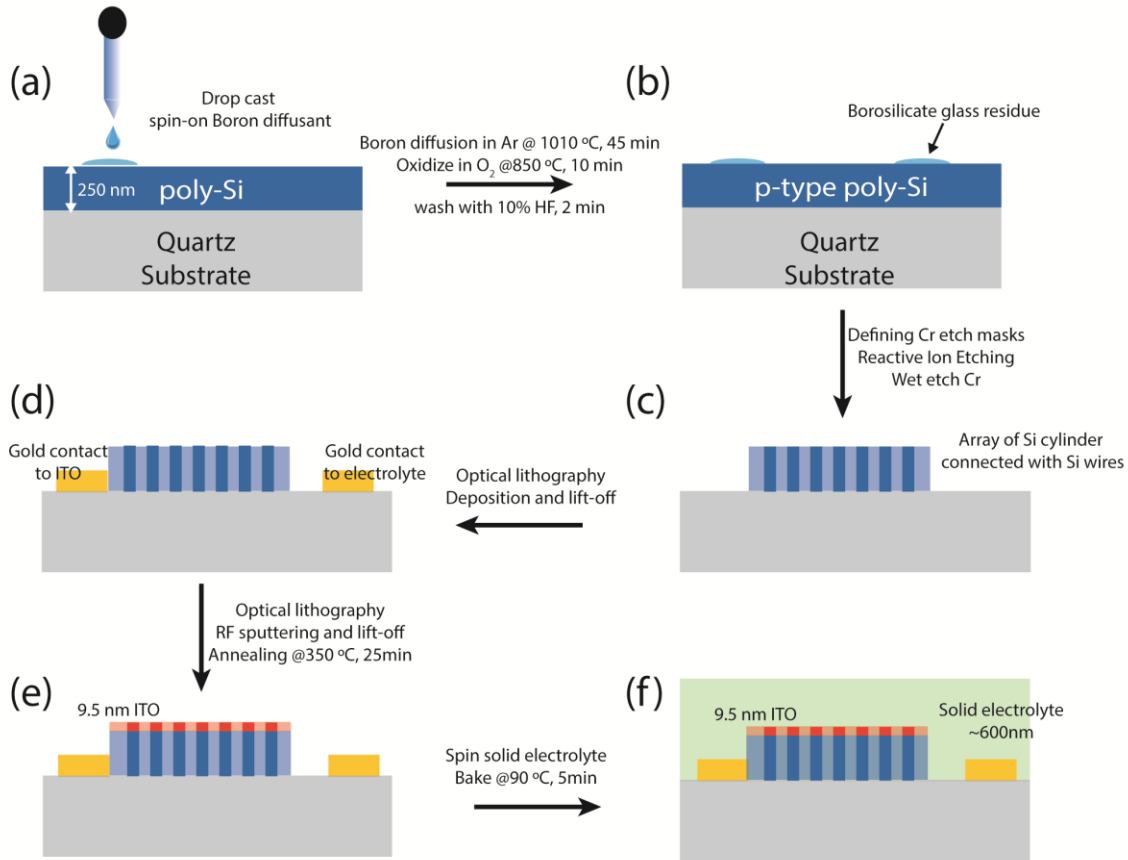
Figure 3.6. (a-b) Doping of the poly-Si film with spin-on Boron dopant solution (B153, Filmtronics Inc.) for achieving conductive p-type silicon. (c) Definition of the silicon resonators array. EBL was first performed to define a Cr etch mask, followed by the deposition of Cr and lift-off. Reactive ion etching was then used to create the silicon structures, Cr is then etched using wet etching. (d) Definition of 60 nm gold electrodes using optical lithography, deposition and lift-off. (e) ~9.5 nm ITO was defined using optical lithography, RF sputtering and lift-off, followed by the annealing of ITO at 350 ℃ for 25 min. (f) Spin-coating of the solid electrolyte on top of the device.

The fabrication process of the proposed device is schematically shown in Figure 3.6. We started with polycrystalline silicon (poly-Si) that is deposited on a quartz wafer via low-pressure chemical vapor deposition (LPCVD). To ensure that the ITO films on top of the silicon cylinders are electrically connected, the poly-Si was then doped with boron by using the diffusion of boron at 1010 ℃. The Cr patterns that were used as reactive ion etching (RIE) masks were then fabricated on top of the doped poly-Si by

42

standard electron beam lithography (EBL), deposition and lift-off processes. RIE was then performed to create the array of the silicon cylinders and the silicon wires, with an array size of 50 x 50 μm. Cr was then removed by wet-etching, followed by two steps of optical lithography, deposition and lift-off processes to define the 60 nm thick gold contacts and the ITO thin film that covers only the resonator array. The as-deposited ITO has thickness of 9.5 nm which is slightly larger than the design. A microscope image of the fabricated device is shown Figure 3.7(a), and the SEM image of the silicon resonators before the deposition of ITO is shown in Figure 3.7(b).
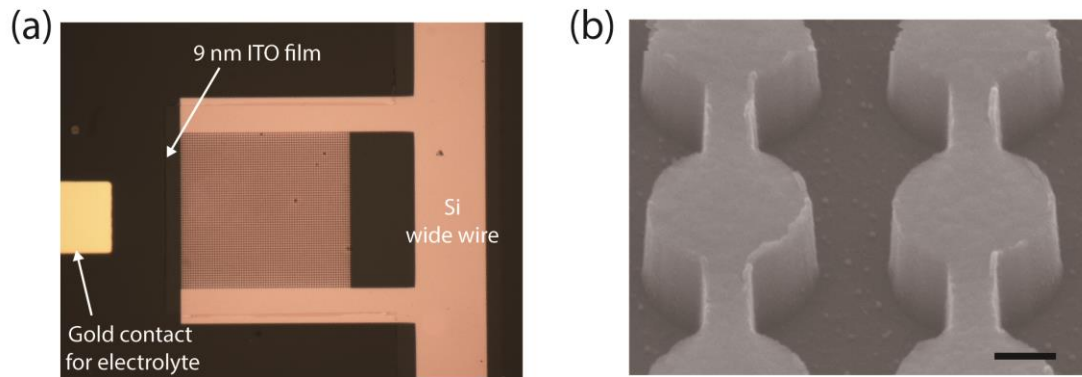
Figure 3.7. (a) Microscope image of the fabricated device consisting of a 50 μm x 50 μm array of silicon resonators and wires. Each array is connected by wide silicon buses to electrically access each element, ~9.5 nm ITO can be seen from edge of the ITO films. (b) SEM image of the resonator, the scale bar is 200 nm.

As was introduced in Chapter 1, to dynamically modulate the optical properties of ITO, an electrostatic gate needs to be applied to modify the carrier concentration inside ITO, which in turn results in a large shift of the plasma frequency[56]. To demonstrate modulation using the ITO-integrated dielectric metasurface we used a solid electrolyte that can be easily spin-coated on top of the ITO surface as the gate. The solid electrolyte we used was composed of bis(trifluoromethylsulfonyl)amine lithium salt ($CF_3SO_2NLiSO_2CF_3$) dissolved in poly(ethylene oxide) (PEO), with the recipe being

adopted from ref [115]. The mechanism of modulation is shown in Figure 3.8(a). When a

positive bias is applied, due to the formation of the electric double layer at the interface,

positive charges are attracted to the top surface of ITO, resulting in carrier depletion in

ITO and thereby a red-shift of its plasma frequency.
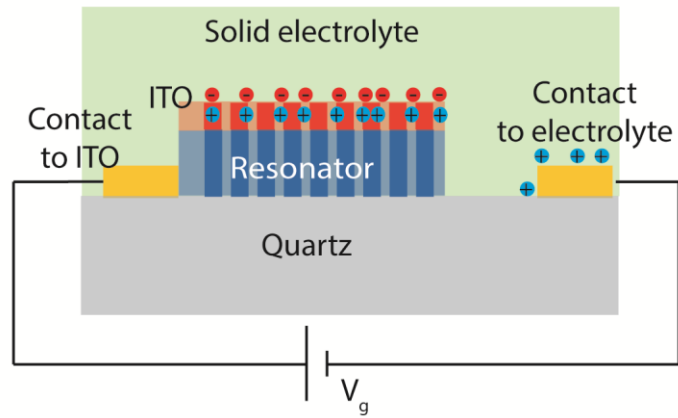
Figure 3.8. Mechanism of modulating ITO carrier density using a solid electrolyte.
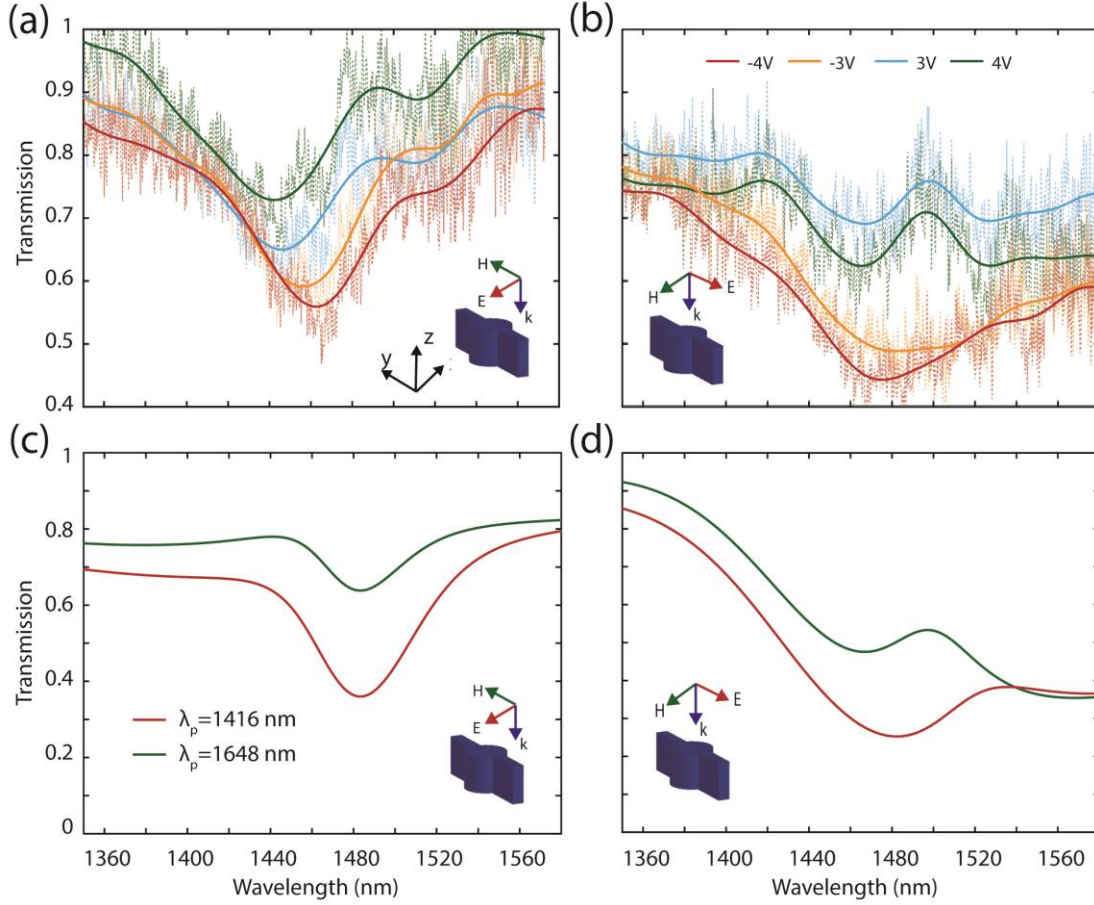
Figure 3.9. (a) Experimental modulation of ITO-Huygens' surface for E_x polarization. (b) The modulation for E_y polarization. (c) Simulation of the transmission when ITO is under accumulation and depletion. The corresponding plasma wavelengths are 1416 nm and 1648 nm, respectively. The electric field has the E_y polarization. (d) Same simulation in (c) for E_x polarization.

The preliminary experimental modulation results are presented with dashed lines in Figure 3.9(a, b). Since the noise is high due to the limited signal intensity, numerically smoothed curves are drawn as guides to the eye. It can be seen that 25%-30% modulation in absolute transmission was obtained from both E_x and E_y polarizations when the voltage was tuned from -4V to 4V, which correspond to the processes when carrier are injected into or depleted from ITO, respectively. The plasma wavelength of ITO before modulation is about 1500 nm, with a carrier concentration of 6.9×10^{20}/cm^3 obtained from $n_0 = \varepsilon_0 m^* \omega_p^2 / e^2$, where $m^* = 0.35 m_0$ is the effective mass of ITO[82]. The change of

ITO carrier concentration upon gating can be estimated using $\Delta n = CV = 2.2 \times 10^{13}/cm^2$, where $C = 0.88\,\mu F/cm^2$ is the capacitance of the same solid electrolyte[115]. As such, the carrier concentration in ITO under depletion and injection is calculated to be $5.9 \times 10^{20}/cm^3$ and $7.9 \times 10^{20}/cm^3$, corresponding to plasma wavelengths at 1648 nm and 1416 nm, respectively.

This estimation does not take the thickness of the depletion/accumulation layer, which should be much smaller than 9.5 nm[59], into consideration. However, the simple calculation mimics the real system to some degree if the carrier distribution within the ITO film can be approximated with an effective carrier density calculated above. Transmission simulations at the calculated carrier concentrations are shown in Figure 3.9 (c-d), showing a modulation depth only slightly larger than the experiment results, implying that the estimation can be used to approximate the much more complicated real system. However, more careful characterization of the change in ITO carrier density upon electrostatic gating still needs to be performed, which can be done using electrical Hall measurements.

Other reasons that could lead to the degradation in performance include the angle of incidence during the measurement as well as large noise in the experiments. The angular sensitivity of our metasurface mainly results from the thin silicon wires, and the transmission varies significantly with increasing angle of incidence for the p-polarization when the incident electric field is polarized in the y direction (Figure 3.10b). To eliminate the higher incident angles contained in the focused beam, we closed the back aperture on the incident objective. As a result, the total intensity is very low, leading to high noise in the data. It also needs to be noted that the modulation for the two polarizations does not

match well with each other, with a saturation of modulation at negative voltages for E_x polarization and positive voltages for E_y polarization. This inconsistency can be attributed to the slow response of the solid electrolyte as a long time is needed for the ions to move and form a gate at the ITO surface, especially at high voltages.
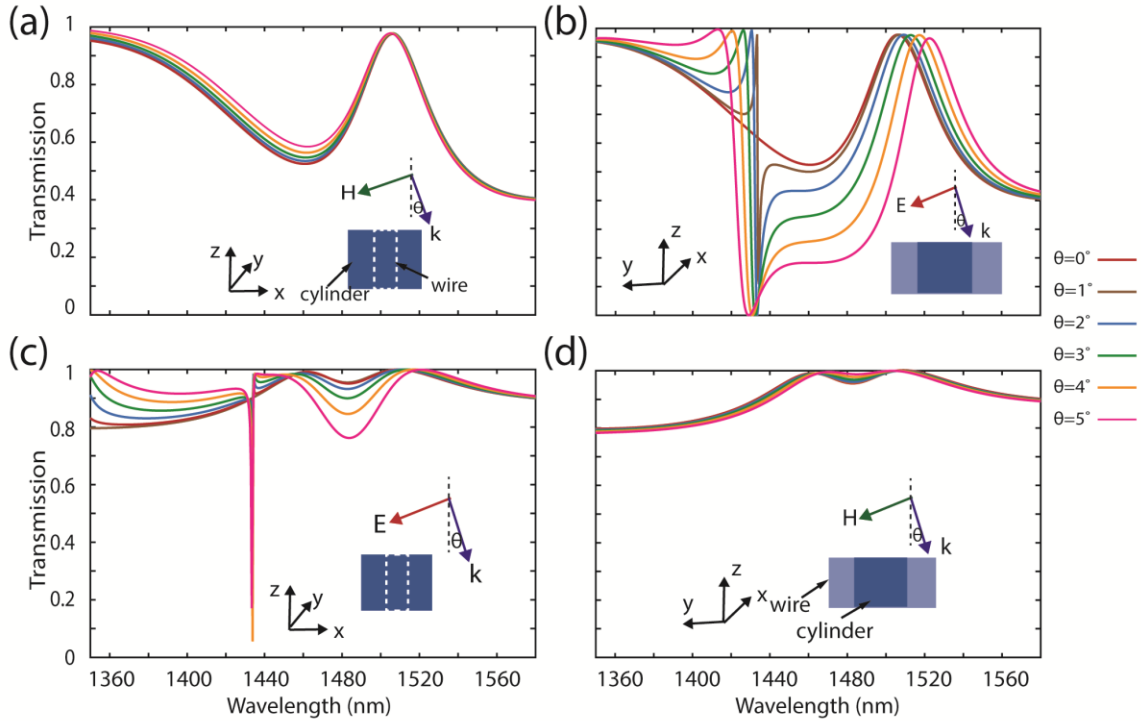
Figure 3.10. Angular response of the Huygens' metasurface for s and p polarizations when incident electric field is along x or y direction. (a) s-polarized light with electric field incident along y direction. (b) p-polarized light with electric field incident along y direction. (c) p-polarized light with electric field incident along x direction. (d) s-polarized light with electric field incident along x direction.

3.6 Conclusion

In summary, we demonstrated for the first time the integration of ITO with dielectric metasurfaces and the active modulation of light based on the dynamic tuning of the carrier concentration in ITO. The absence of material absorption in dielectric resonators eliminates the parasitic loss in the device, thus allowing all the absorption to happen solely in the ITO, enabling high efficiency in absorption modulation. The use of a

Huygens' metasurface leads to over 70% on-state transmission in the simulation and the overlap of the strongly enhanced out-of-plane electric field from the Huygens' mode with the ENZ mode results in greatly enhanced light-matter interactions in ITO, leading to about 45% transmission modulation based on simulations while modulation of 25% to 30% has been demonstrated in preliminary experiments. However, devices with thinner ITO films and more controllable solid electrolytes are needed for better device performance. Moreover, the noise in the measurements needs to be eliminated, which can be achieved by increasing the intensity of the incident light during the measurement. Also, the carrier density change as a function of the gate voltage needs to be electrically characterized in order to fully understand the experimental data. Although a solid electrolyte is used in the experiments as a first demonstration, solid-state gating can be achieved by thermally grown silicon dioxide on structured silicon nano-cylinders for practical use of the device.

Chapter 4

Enhanced Photodetection in Bilayer MoS$_2$ via Hot Electron Injection

4.1 Introduction

In this Chapter, we introduce a different approach to achieving strong photoresponse in 2D materials using hot electron injection. Compared to the approaches that aim at creating modal overlap, as was introduced in Chapter 2 and Chapter 3, the technique of hot electron injection enables the capture of photons with energy lower than the bandgap of the semiconductor[116]–[118]. In addition to the demonstration of hot electron injection into bulk semiconductors such as silicon[23], [24], [119] VO$_2$[21] and TiO$_2$[120], the injection of hot electrons into two-dimensional (2D) materials such as graphene[121] and MoS$_2$[22], [122] has also been demonstrated, providing additional doping [123] or inducing structural and phase transitions[22]. For photodetection, MoS$_2$ is an particularly attractive hot electron acceptor due to its semiconductor electronic band structure and internal photogain owing to the various traps at the metal/MoS$_2$ and/or MoS$_2$/substrate interfaces[70], [124].

In this chapter, we combine the technique of hot electron injection and the photoamplification effect in MoS$_2$ in realizing a below-bandgap photodetector with high responsivity. We perform an extensive investigation on the injection of hot electrons into a bilayer MoS$_2$ film that has been integrated with plasmonic resonators. With an asymmetric plasmonic structure, we demonstrate sub-bandgap photoresponse and a photocurrent spectrum that varies with the bias polarity, features that are explained by the hot electron injection and the trap induced photoamplification. We verify the presence of hot electron injection by examining control devices in which an injection barrier layer is

49

used to distinguish the relative contribution of hot electron injection and photothermoelectric effects[125], [126]. The hot electron injection efficiency is estimated to be comparable with Si-based hot electron photodetectors[23] while a photocurrent amplification factor of 10^5 results in a photoresponsivity of 5.2 A/W under 1070 nm illumination, which is far above similar silicon-based hot electron photodetectors in which no photoamplification is present.

4.2 Plasmonic Structure Design and Fabrication

The hot electron photodetectors are typically realized based on the injection of electrons generated from plasmon resonances in metallic nanostructures into an adjacent semiconductor. A Schottky barrier at the metal/semiconductor interface is usually used to prevent the backflow of electrons while an Ohmic contact on the other end of the semiconductor is needed to collect the injected electrons and generate photocurrent[27]. This process was introduced in chapter 1 and the schematic is presented again in Figure 4.1, showing that both a Schottky contact and an Ohmic contact are required to acquire photocurrent when no bias is applied.
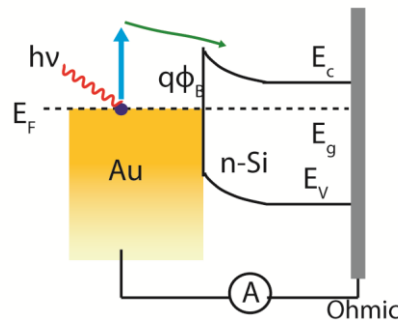
Figure 4.1. Band diagram of a typical hot electron photodetector based on silicon.

In our device, instead of using asymmetric junctions, we design an asymmetric plasmonic structure that generates different amounts of hot electrons in the source and

drain electrodes. As is shown in Figure 4.2(a), the interdigitated asymmetric plasmonic structure consists of resonant wires and non-resonant wires. The non-resonant wires (NRWs, color coded with green for clarity) are narrow (w_2 =80 nm) such that the resonance modes are outside the wavelength range of the measurement, while the resonant wires (RWs, color coded with yellow) have antennas with a dipolar resonance at 1250nm (a =280 nm, b =125 nm, p =340 nm, w_1 =90 nm) when illuminated with the electric field oriented along the y-direction (E_y, see Figure 4.2). In this case, zero-bias current is generated due to the fact that the resonant wires generate far more electrons than the non-resonant wires.

During device fabrication Au structures are first defined on a piranha (3:1 H_2SO_4:H_2O_2) cleaned quartz substrate using electron beam lithography (EBL) and deposition of 2 nm Ti and 15 nm Au films. Thick Au contacts were then fabricated using a second lithography step. The device was cleaned for a second time with O_2 plasma (30s) and piranha (1 min) to ensure a pristine Au surface. Bilayer MoS_2 that was mechanically exfoliated on a PDMS template was then transferred on top of the Au structures using a stamping method[115], [127], more details regarding the transfer process can be found in Appendix 1. During fabrication, we found that the device yield when utilizing bilayer MoS_2 was higher than that for monolayer devices, which is likely due to the higher stiffness of the bilayer films[128]. Because of that, only bilayer MoS_2 devices are examined here, although we believe that injection of hot electrons and photocurrent amplification should also be observable in monolayer MoS_2 due to their similar electronic band structures. After annealing in a H_2/Ar environment at 160 ℃ for 30 min to further

remove any polymer residue the device was wire bonded and loaded into a vacuum

chamber for measurements.
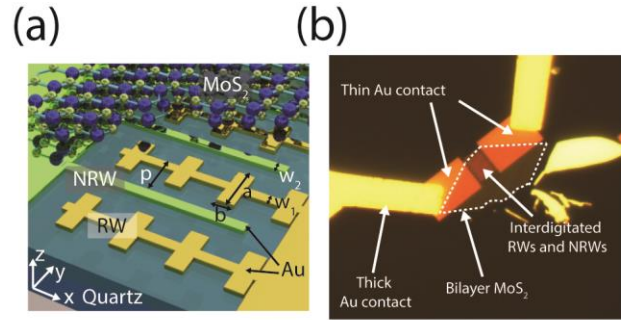
Figure 4.2. (a) Schematic of the asymmetric plasmonic device in which the yellow Au structures (RWs) are resonant while the green Au structures (NRWs) are non-resonant. (b) Microscope image of the device with bilayer MoS_2 on top of the thin Au structures.

4.3 Photoresponsivity Spectrum
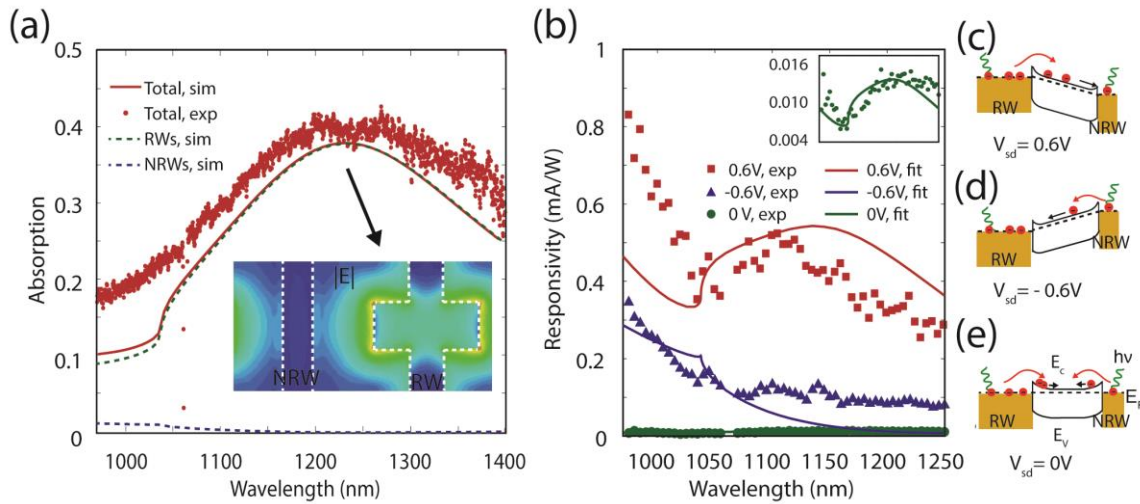
Figure 4.3. (a) The experimental and simulated absorption spectra of the asymmetric structure illuminated with E_y polarization (red dots and line). The green and blue dashed lines are the absorption in the RWs and NRWs, respectively. The inset shows the electric field distribution ($|E|$) at the resonance peak. (b) Responsivity under E_y polarization at 0.6V, -0.6V and 0V biases (red, blue, and green dots, respectively). The solid lines are the fit to the data. The inset is a zoom-in of the photocurrent and the fitting at 0V bias. (c-e) Band diagrams for the device under 0.6V, -0.6V and 0V bias.

The experimental and simulated absorption spectra of the entire structure are

shown in Figure 4.3(a) and the simulated absorption in the individual components (RWs

and NRWs) are shown with dotted lines. It can be seen that the RW component exhibits a

strong resonance under E_y polarized excitation as is evident in the electrical field profile

(/E/) shown in the inset, while there is no such resonance in the NRW component. The

experimentally measured photocurrent spectrum is shown in Figure 4.3(b) for source-

drain biases of 0.6V, -0.6V, and 0V (red, blue and green dots). These measurements were

obtained with a chopper operating at 387 Hz and a lock-in amplifier. As can be observed,

the photoresponsivity peaks at 1120 nm for 0.6V bias but disappears when the bias is -

0.6V. This observation can be understood by the fact that for E_y polarized excitation the

RW components dominate the hot electron generation due to their higher optical

absorption. As illustrated with energy band diagrams in Figure 4.3(c) to 2(e), at 0.6V

bias only the hot electrons in the RWs are injected into MoS_2 (Figure 4.3c), resulting in

the responsivity peaking at the RW resonance. For the case of -0.6V bias only hot

electrons generated in the NRWs are injected (Figure 4.3d) and thus the photoresponse

spectrum shows no resonant feature. When there is no bias (0V), hot electrons in both

RWs and NRWs are injected in opposite directions, therefore the net photocurrent will be

proportional to the absorption difference between the RW and NRW components (Figure

4.3e). It should be noted that the 0V and ±0.6V bias conditions also exhibit different gain

levels, which will be discussed later, leading to much lower photocurrent in the un-biased

condition.

The spectrum of the responsivity, $R^i(\omega)$, with the superscript i denoting the

three cases of V_{sd} (0.6V, -0.6V and 0V), can be understood with the following expression,

$$R^i(\omega) = \left[C_f \frac{(\hbar\omega - q\phi_B)^2}{\hbar\omega} \right] \left[k_1 \alpha_{RW,L_d}(\omega) + k_2 \alpha_{NRW,L_d}(\omega) \right] g^i \qquad (4.1)$$

Here, the first bracket is Fowler's formula, which describes the internal quantum efficiency of the photoemission process[26], [129], $\hbar\omega$ is the photon energy, $q\phi_B$ =0.67 eV is the Schottky barrier height between Au and bilayer MoS_2[130] and C_f is a device specific constant that is treated as a universal fitting constant for the three source-drain voltages here. The second bracket represents the probability of a hot electron being generated and transported to the interface, where α_{RW,L_d} and α_{NRW,L_d} are the absorption in RW and NRW, respectively. Due to the limited hot electron diffusion length (L_d ~20 nm[131] at the electron energy considered here), hot electrons generated beyond 20 nm from the structure's edge will not arrive at the Au/MoS_2 interface, preventing injection into the channel. Therefore, only the absorption in Au that occurs within 20 nm to the edge is used in the calculation of α_{RW,L_d} and α_{NRW,L_d} (refer to Appendix 2 for the spectrum of α_{RW,L_d} and α_{NRW,L_d}). The values for (k_1, k_2) are chosen to be (1, 0) for $V_{sd} =$ 0.6V, (0, -1) for V_{sd} = -0.6V and (1, -1) for V_{sd} = 0V bias. The last fitting parameter g^i represents a photogain that depends on the source-drain voltage and will be discussed in later sections. In Figure 4.3(b) we present the fit of equation 1 to the photocurrent spectra (lines), demonstrating good agreement with the line shape of the experimental measurements. The slight discrepancy between the experiments and theory can largely be attributed to fabrication imperfections, the uncertainty in the Schottky barrier height, and the error in estimating the electron diffusion length, L_d. Given the uncertainty in the electron diffusion length we calculated α_{RW,L_d} and α_{NRW,L_d} for L_d values ranging from 10 to 40 nm (Appendix 2). However, the spectral shape of α_{RW,L_d} and α_{NRW,L_d} vary only

slightly with changing L_d values indicating the parameter is not a critical factor in achieving agreement with the experimental data. Another factor that could influence the fitting is the constant C_f, which is generally a function of the wavelength and the profile of the plasmonic resonant mode. As such, it likely varies at short wavelengths where a grating mode is excited in addition to the dipolar mode in the antennas. The absorption spectrum and the photoresponse for illumination polarized along the x-direction (E_x polarization) can be found in Appendix 3. Neither RW nor NRW component responds to E_x polarization and therefore the absorption is minimum due to the lack of resonances. However, similar variations in the photocurrent magnitude under different bias polarities can still be observed although no resonance features are observed.

4.4 Photoresponsivity and Photogain
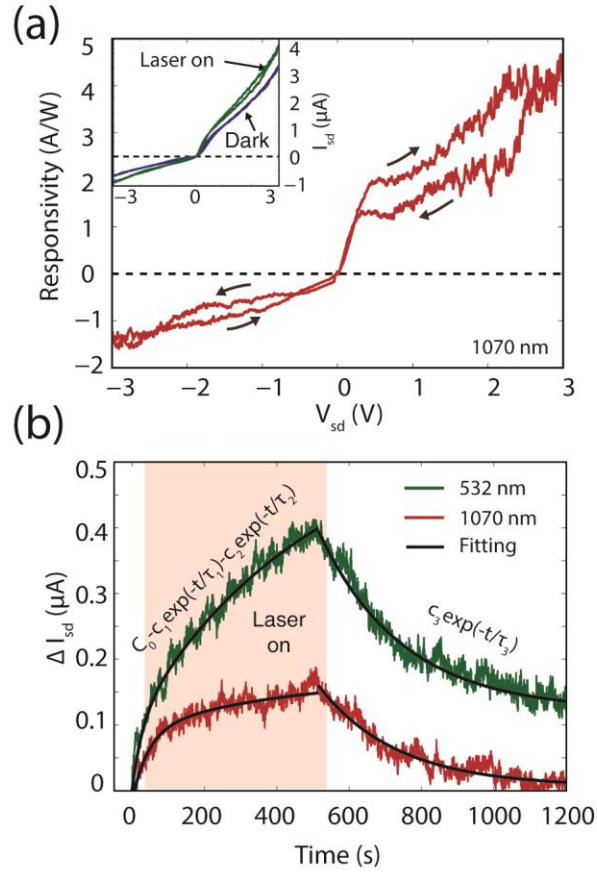
Figure 4.4. (a) The photoresponsivity as a function of source-drain voltage (V_{sd}) measured at 1070 nm under E_y polarization. The inset shows the source-drain current (I_{sd}) as a function of V_{sd} under illumination and in a dark environment. (b) Time response of ΔI_{sd} when illuminated a 1070 nm (red) and 532 nm (green) under 0.8V bias. The laser was turned on at 0s and turned off at 500s. Black curves are the fitting to the experimental curves.

incident	growth		decay
wavelength	τ_1 (s)	τ_2 (s)	τ_3 (s)
1070 nm	44.5	404.7	216.5
532 nm	28.5	494.3	232

Table 4.1. Fitted time constants for the growth and decay regime of the time response under 1070 nm and 532 nm illumination.

As mentioned previously, ultrathin MoS_2 can exhibit photoamlification due to traps at the interfaces[70], [124]. To explore this effect we recorded the change of photoresponsivity as a function of source-drain voltage V_{sd} under illumination with a 150 nW E_y polarized 1070 nm laser (Figure 4.4a). The measurements show increasing responsivity with increasing V_{sd} and a peak responsivity of 4.5A/W at 3V bias. The responsivity was obtained by comparing the difference in source-drain current I_{sd} under illumination and in a dark environment, as is shown in the inset of Figure 4.4(a). The sweeping speed of V_{sd} was kept at 0.02V/s, and the hysteresis in the I_{sd} under illumination indicates the existence of carrier traps in the system, which is the cause of the photocurrent amplification.

To characterize the lifetime of the traps states and gain insight into the photogain mechanism and hot electron injection efficiency, we compared the response of the structure at visible and infrared frequencies. Specifically, we recorded the time response of ΔI_{sd} under a source drain bias of 0.8V and 1070 nm illumination (red curve in Figure 4.4b) and compared it with the well understood[70] photovoltaic effect dominated photoresponse under 532 nm illumination (green curve). During the experiment, the laser was kept on for 500s and then turned off so that the entire rise and decay processes of ΔI_{sd} were recorded. For both 1070 nm and 532 nm excitation, the photocurrent as a function of time can be expressed as,

$$I_{PC}(t) = \Delta I_{sd}(t) = V_{sd} \frac{\partial G}{\partial n} \Delta n(t) = V_{sd} \frac{\partial G}{\partial n} \begin{cases} \int_0^t (dn/dt)dt, & (0 < t < 500) \\ I_{t=500} - \int_{500}^{t-500} (dn/dt)dt, & (t > 500) \end{cases} \quad (4.2)$$

57

where G is the conductance, $V_{sd} \left(\partial G / \partial n \right)$ is the previously mentioned photogain g, n is the number of electrons in MoS$_2$, and dn / dt is the rate at which carriers appear due to hot electron injection or photogeneration. For the case of 1070 nm illumination, this rate can be expressed as $dn / dt = N_{inj} - n / \tau$ for the growth region during $0 < t < 500$s and $dn / dt = -n / \tau$ for the decay regime at $t > 500$s, where N_{inj} is the rate of hot electron injection and τ is the effective trapping lifetime. As can be observed in Figure 4.4(b), the growth region is composed of two exponential terms, indicating two carrier trapping mechanisms in the system. In contrast, in the decay region one exponential term dominates. The fitting of the growth and the decay of the photocurrent are shown with black lines in Figure 4.4(b), with the fitted time constants presented in Table 4.1. The close match of the time constants for 1070 nm and 532 nm illumination indicates the same trapping mechanisms for both above and below bandgap illumination and thereby confirms that the two processes should share the same photogain. Normalizing ΔI_{sd} with incident power (35 pW for 532 nm and 150 nW for 1070 nm), we obtain a responsivity of 1.1×10^5 A/W at 532 nm and 5.2 A/W at 1070nm. Since MoS$_2$ absorbs ~25% due to the plasmon enhanced absorption at 532 nm, obtained through simulation, we infer a photogain (g) of 1.05×10^5 at 0.8V bias. The external hot electron injection efficiency η_{ext} is estimated to be 1.40 $\times 10^{-4}$, which was obtained using the relationship $\eta_{ext} = R / \left(A * g \right)$, with R and A being the photoresponsivity and the total absorption at 1070 nm, respectively. The injection efficiency is comparable to Si-based hot electron photodetectors[23] in which Au antennas are placed on top of silicon. While this efficiency is low, the device presented here is not optimized for maximum photocurrent.

Numerous techniques that have been demonstrated to improve injection efficiency in silicon-based devices could readily be applied to 2D materials such as MoS_2[24], [29], [132].

4.5 Control Experiment
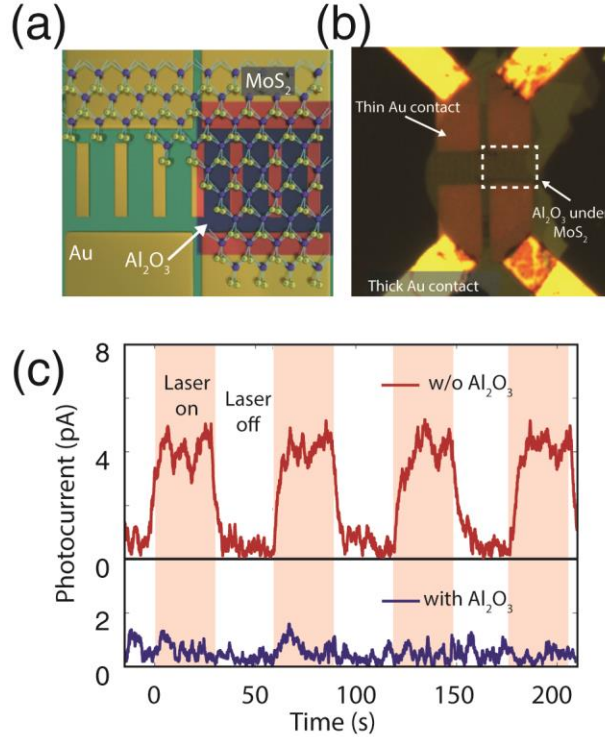
Figure 4.5. (a) Schematic of the control device. On the left sub-device MoS_2 is in direct contact with Au while in the right sub-device a 10 nm film of Al_2O_3 is present between MoS_2 and Au. (b) Microscope image of the device. (c) Photocurrent measured from the left (upper panel) and the right (lower panel) sub-device. The laser power was 364 nW at 1150 nm when measuring the MoS_2/Au sub-device and 170 nW at 1080 nm when measuring the MoS_2/Al_2O_3/Au sub-device.

In order to elucidate the role of photothermoelectrical effects[125], [126] to the photocurrent we fabricated a control device composed of two individual sub-devices sharing the same MoS_2 flake (Figure 4.5 a, b). In one sub-device (right hand side, Figure 4.4a, b) we deposited a 10 nm thick Al_2O_3 film before transferring the MoS_2, while the other sub-device (left hand side, Figure 4.5 a, b) has no such coating. The Al_2O_3 serves as

a barrier for hot electron injection though the injection barrier is thin enough to ensure that the temperature profile on MoS_2 is similar for both sub-devices. Identical Au wires with a width of 210 nm are arranged with a period of 830 nm, forming a grating with a plasmon resonance at ~1150 nm for the polarization perpendicular to the grating direction. Figure 4.5(c) shows the photocurrent from the left and right devices obtained at an identical source-drain voltage of $V_{sd} = 0.7V$. In addition to using a chopper and lock-in amplifier, we modulated the laser on and off using another shutter at a cycle of 60s such that the photocurrent signals from the lock-in amplifier can be distinguished from the noise. While the sub-device with the Al_2O_3 barrier exhibits no noticeable photocurrent, the sub-device without Al_2O_3 exhibits a clear photoresponse. Considering the fact that the two sub-devices have the similar plasmonic heating temperature profiles, these measurements further indicate that the photothermoelectrical effects are negligible compared with hot electron injection at the illumination intensities employed. The photovoltaic effect is not considered here since the bilayer MoS_2 has an indirect bandgap at 750 nm (1.65 eV)[133], much shorter than the illumination wavelength range of interest.

4.6 Conclusion

As a summary, we have extensively studied the hot electron induced photocurrent in bilayer MoS_2 in conjunction with plasmonic structures. The ability to operate with below-band gap illumination allows such devices to operate in the telecommunications band and allows flexible tuning of the peak responsivity wavelength. Furthermore, an amplification factor of 1.05×10^5 has led to the highest hot electron-based responsivity values measured to date in this wavelength region.

However, the practical application of our device requires further engineering of the trap states. For instance, a faster time response is typically desired for photodetectors, while decreasing the trapping life time will also lead a reduction in the photoamplification. Therefore, a good trade-off needs to be found between the response time and the photoresponsivity. On the other hand, ideal optical memory devices generally require the ability to store information over long periods of time. In this case, the traps need to be engineered to have an even longer response time and the erasing of signals could be achieved using additional gate pulses[134].

Chapter 5

Conclusion and Outlook

The focus of my PhD research has been to integrate active ultrathin films, especially newly emerged two-dimensional materials and transparent conductive oxide nano films, with properly engineered nano-optical structures such that their interactions with light can be greatly enhanced. The optoelectronic devices demonstrated based on this integration show superior performance in terms of high photoresponsivity and high modulation depth. In this chapter, I will summarize these results as well as give my perspective regarding some potential research directions related to what has been shown in this thesis.

5.1 Conclusion

In Chapter 2, near-unity device absorption was demonstrated by integrating 2D materials with a Fano-resonant photonic crystal (FRPC). Graphene and MoS_2 were implemented in the demonstration. Using photocurrent measurements, 77% absorption was experimentally achieved in graphene, which corresponds to a 33 times absorption enhancement. Simulations show that a maximum of 95% absorption can be achieved in more lossy 2D materials at visible ranges. Therefore, this structure can also be implemented with other ultrathin materials in which the light-matter interaction is limited due to limited interaction length.

Chapter 3 detailed an experimental demonstration of an active light modulator by combining a TCO nano-film exhibiting an epsilon-near zero mode with dielectric

Huygens' metasurfaces. The strongly enhanced electric field together with the absence of non-radiative decay in the silicon resonators results in a transmission modulation of about 45%. Preliminary experimental results were presented and are explained with simulations.

In Chapter 4, I introduced a hot electron-based photodetector using bilayer MoS_2. Below bandgap photodetection in the bilayer MoS_2 was demonstrated with a photoamplification over 10^5 and photoresponsivity of 5.2A/W. The integration of bilayer MoS_2 with the technique of hot electron injection enabled the realization of near infrared sub-bandgap photodetection with photogain, and the measured photoresponsivity is far above similar silicon-based hot electron photodetectors in which no photoamplification is present.

5.2 Challenges and Outlook for Ultrathin Film-based Optoelectronics

The development of new optoelectronic devices with high performance is a topic related to multiple disciplines. On one hand, novel optical structures could potentially lead to a boost in various kinds of optoelectronic devices. On the other hand, the realization of high performance devices relies on developments within material science in discovering exciting new materials and properties. Up to the present, although two-dimensional materials have been demonstrated to have promising optoelectronic properties, further technological improvements are still needed to achieve optoelectronic devices that outperform traditional devices based on bulk semiconductors in terms of response time, responsivity, and bandwidth. More importantly, commercial applications of two-dimensional materials require the development of robust large-scale fabrication techniques that can repeatability produce uniform high-quality 2D materials at a low cost.

However, we believe the growing field of 2D materials will eventually provide us solutions to all these challenges.

In addition to the applications demonstrated in this dissertation, below I propose some potentially interesting directions that could improve the performance of 2D material-based optoelectronic devices via the integration with nano-optical structures.

The recent advances in achieving near-unity quantum yield in monolayer MoS_2 by eliminating defects with a superacid treatment[51] provides exciting opportunities in realizing high-efficiency light-emitting diodes (LEDs) and lasers based on transition metal dichalcogenides (TMDCs) and their heterostructures. To efficiently collect the emitted photons, the TMDCs need to be integrated with dielectric cavities or resonators. In addition to the dielectric structures introduced in Chapter 1, Mie resonances that are capable of manipulating the electric field orientation as well as the far field emitting pattern can be used. The ability to manipulate the electric field is particularly important in enhancing interlayer exciton emission that exists in vertical heterojunctions such as MoS_2/WS_2. These interlayer excitons are primarily orientated out-of-plane, as such, the majority of the emitted light propagates in the in-plane direction, prohibiting efficient light collection from the top of the film. The utilization of the Mie resonances, however, provides possibilities in tailoring the electric field orientation using the electric and magnetic resonances. By overlapping the electric field orientation with the out-of-plane interlayer dipoles, the emitted photons can thus be efficiently collected from the top.

The interactions between TMDCs and hot electrons injected from plasmon resonances have been demonstrated to be intriguing. The injection of hot electrons into the conduction band of monolayer MoS_2 has been shown to be capable of inducing a

phase transition through the population of the Mo 4d orbitals[22]. Based on the large permittivity difference between MoS_2's semiconductor 2H phase and the metallic 1T phase [135], an all-optical modulator can be realized via the integration with a properly engineered plasmonic structure that exhibits a strongly enhanced electric field at the probe wavelength as well as an efficient hot electron injection at the pump wavelength.

Other than inducing a phase transition, hot electron injection assisted up-conversion is also an interesting topic to investigate. The hot electron assisted up-conversion in quantum wells[136] has been proposed. In this process an electron with initial energy much lower than the Fermi level can absorb two photons and end up with sufficient energy to cross over the Schottky barrier at the metal/semiconductor interface. The hot electrons eventually end up in the conduction band of the quantum well, followed by the recombination and the emission of photons with energy higher than the excitation wavelength of the surface plasmon resonance. The similar mechanism can also be applied to the TMDCs. Compared to quantum wells, the TMDCs are more cost-effective and easy to fabricate, making the system flexible and suitable to various substrates.

TCOs have recently garnered interest in the field of nanophotonics with the theoretical prediction[112] and experimental demonstration[105] of the epsilon-near zero (ENZ) mode in thin films. The wide tunability of TCOs' plasma frequency in the near-infrared and infrared ranges together with the strongly enhanced electric field in the ENZ mode has opened opportunities for efficient modulation of light. Moreover, with the integration of metasurfaces that possess various functionalities, people can realize active modulators with the ability to control the intensity, phase, spin/orbital angular momentum

in transmission, reflection, and emission. Moreover, based on existing mature fabrication techniques, various TCOs-based optical modulators can be expected to be commercialized in the near future.

Appendix: Hot Electron Photodetection

1.   The exfoliation and transfer of MoS$_2$

The exfoliation and transfer followed the process described in Prasai et al.[115]. The target substrate with the fabricated Au structure was first cleaned with O$_2$ plasma for 30s and piranha (3:1 H$_2$SO$_4$: H$_2$O$_2$) for 1 min to ensure a pristine surface. To transfer MoS$_2$, we followed the recipe developed by Zomer et al.[127]. Elvacite polymer (~1μm thick) was first spun onto a PDMS/clear Scotch tape sandwich structure and the structure was baked at 90°C for 5mins. Bilayer MoS$_2$ was exfoliated onto Elvacite and verified using optical microscopy and Raman spectroscopy[137]. Bilayer MoS$_2$ was then aligned with Au electrodes using an optical microscope and brought into contact with the Au at 120°C. The PDMS/polymer layer was then mechanically separated from the MoS$_2$ stack at 80°C. To remove the polymer residues, the device was soaked in acetone for 30 min and rinsed in IPA.

2.   The absorption within electron diffusion length (L_d) to the structure edge

In Figure A.1 we show the normalized absorption spectrum (α_{RW,L_d} and α_{NRW,L_d}) in Au within one diffusion length (L_d) of the structure's edge. Due to the inaccuracy in estimating L_d, in Figure A.1 we considered diffusion lengths ranging from 10 nm to 40 nm. While L_d = 20nm is used in the fitting of the photoresponsivity spectrum in the manuscript, different L_d values result in minor changes to the spectral lineshapes. It needs to be noted that the resonant feature appear at ~1050 nm in the spectrum of α_{NRW,L_d} is due to the grating resonant mode in the array.
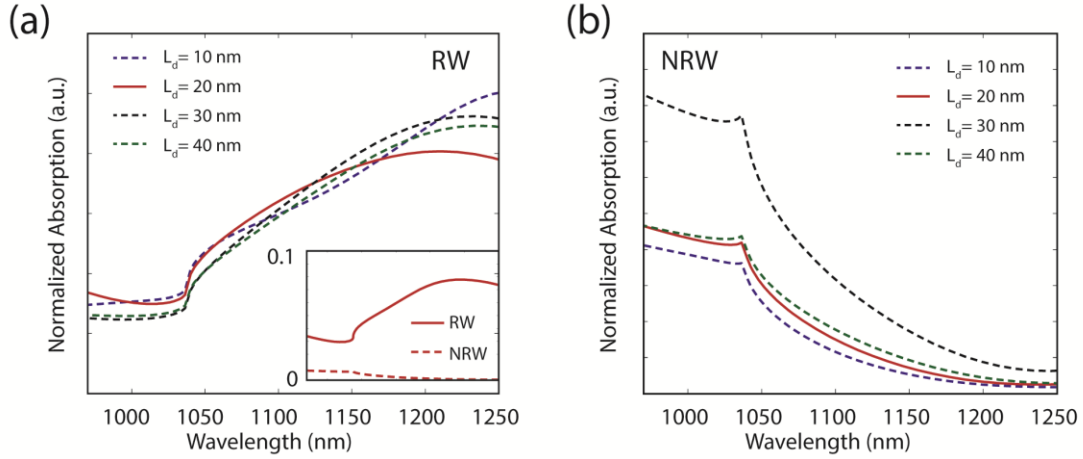
Figure A.1. Normalized absorption spectrum α_{RW,L_d} (a) and α_{NRW,L_d} (b) for electron diffusion length L_d ranging from 10 to 40 nm. The curve corresponding to $L_d = 20$ nm (the solid line) is used in the fitting of the photoresponsivity in the main text. The normalization factor for the (a) and (b) are the same. The inset in (a) shows the absolute value of α_{RW,L_d} and α_{NRW,L_d} when $L_d = 20$ nm.

3.   The absorption and photoresponsivity for E_x polarization
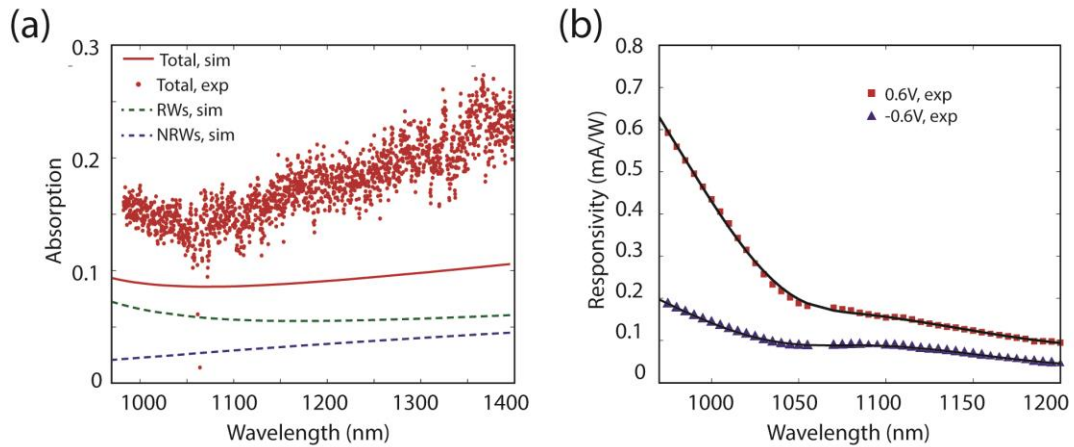
Figure A.2. (a) Experimental and simulated total absorption with E_x polarized excitation. The green and yellow dashed lines are the simulated absorption in RW and NRW components. (b) Photoresponsivity spectrum with measured with E_x polarized excitation at 0.6 V and -0.6V biases. The black lines are the guide to the eye.

The absorption and the photoresponsivity for the E_x polarization are shown in Figure

A.2. No resonant behavior can be seen because neither RW nor NRW component

68

responds to the E_x polarized light. However, a similar trend of photoresponsivity spectrum can be seen, showing higher photoresponsivity at short wavelengths.

References

[1]   P. M ühlschlegel, H.-J.-J. Eisler, O. J. F. Martin, B. Hecht, and D. W. Pohl, "Resonant Optical Antennas," *Science (80-.).*, vol. 308, no. 5728, pp. 1607–1609, 2005.

[2]   D. K. Gramotnev and S. I. Bozhevolnyi, "Plasmonics beyond the diffraction limit," *Nat Phot.*, vol. 4, no. 2, pp. 83–91, Feb. 2010.

[3]   J. A. Schuller, E. S. Barnard, W. Cai, Y. C. Jun, J. S. White, and M. L. Brongersma, "Plasmonics for extreme light concentration and manipulation," *Nat Mater*, vol. 9, no. 3, pp. 193–204, Mar. 2010.

[4]   E. S. Barnard, J. S. White, A. Chandran, and M. L. Brongersma, "Spectral properties of plasmonic resonator antennas," *Opt. Express*, vol. 16, no. 21, pp. 16529–16537, Oct. 2008.

[5]   N. Liu, L. Langguth, T. Weiss, J. Kastel, M. Fleischhauer, T. Pfau, and H. Giessen, "Plasmonic analogue of electromagnetically induced transparency at the Drude damping limit," *Nat Mater*, vol. 8, no. 9, pp. 758–762, Sep. 2009.

[6]   N. Verellen, Y. Sonnefraud, H. Sobhani, F. Hao, V. V Moshchalkov, P. Van Dorpe, P. Nordlander, and S. A. Maier, "Fano Resonances in Individual Coherent Plasmonic Nanocavities," *Nano Lett.*, vol. 9, no. 4, pp. 1663–1667, Apr. 2009.

[7]   S. Zhang, D. A. Genov, Y. Wang, M. Liu, and X. Zhang, "Plasmon-Induced Transparency in Metamaterials," *Phys. Rev. Lett.*, vol. 101, no. 4, p. 47401, Jul. 2008.

[8]   N. Liu, M. Mesch, T. Weiss, M. Hentschel, and H. Giessen, "Infrared Perfect Absorber and Its Application As Plasmonic Sensor," *Nano Lett.*, vol. 10, no. 7, pp. 2342–2348, Jul. 2010.

[9]   N. I. Landy, S. Sajuyigbe, J. J. Mock, D. R. Smith, and W. J. Padilla, "Perfect Metamaterial Absorber," *Phys. Rev. Lett.*, vol. 100, no. 20, p. 207402, May 2008.

[10]   J. A. Dionne, K. Diest, L. A. Sweatlock, and H. A. Atwater, "PlasMOStor : A Metal - Oxide - Si Field Effect Plasmonic Modulator," *Nano Lett.*, vol. 9, no. 2, pp. 897–902, 2009.

[11]   D. K. Gramotnev and S. I. Bozhevolnyi, "Plasmonics beyond the diffraction limit," *Nat. Photonics*, vol. 4, no. 2, pp. 83–91, Jan. 2010.

[12]   J. A. Schuller, E. S. Barnard, W. Cai, Y. C. Jun, J. S. White, and M. L. Brongersma, "Plasmonics for extreme light concentration and manipulation," *Nat. Mater.*, vol. 9, pp. 193–204, Mar. 2010.

[13] W. Srituravanich, L. Pan, Y. Wang, C. Sun, D. B. Bogy, and X. Zhang, "Flying plasmonic lens in the near field for high-speed nanolithography," *Nat. Nanotechnol.*, vol. 3, no. December, pp. 733–737, Dec. 2008.

[14] X. Shi and L. Hesselink, "Mechanisms for Enhancing Power Throughput from Planar Nano-Apertures for Near-Field Optical Data Storage," *Jpn. J. Appl. Phys.*, vol. 41, no. 3S, p. 1632, 2002.

[15] R. F. Oulton, V. J. Sorger, T. Zentgraf, R.-M. Ma, C. Gladden, L. Dai, G. Bartal, and X. Zhang, "Plasmon lasers at deep subwavelength scale," *Nature*, vol. 461, no. 7264, pp. 629–632, Oct. 2009.

[16] H. A. Atwater and A. Polman, "Plasmonics for improved photovoltaic devices," *Nat Mater*, vol. 9, no. 3, pp. 205–213, Mar. 2010.

[17] H. Aouani, M. Rahmani, M. Navarro-Cia, and S. A. Maier, "Third-harmonic-upconversion enhancement from a single semiconductor nanoparticle coupled to a plasmonic antenna," *Nat Nano*, vol. 9, no. 4, pp. 290–294, Apr. 2014.

[18] HaffnerC., HeniW., FedoryshynY., NiegemannJ., MelikyanA., E. L., BaeuerleB., SalaminY., JostenA., KochU., HoessbacherC., DucryF., JuchliL., EmborasA., HillerkussD., KohlM., D. R., HafnerC., and LeutholdJ., "All-plasmonic Mach–Zehnder modulator enabling optical high-speed communication at the microscale," *Nat Phot.*, vol. 9, no. 8, pp. 525–528, Aug. 2015.

[19] S. Mubeen, J. Lee, N. Singh, S. Krämer, G. D. Stucky, and M. Moskovits, "An autonomous photosynthetic device in which all charge carriers derive from surface plasmons," *Nat. Nanotechnol.*, vol. 8, no. 4, pp. 247–51, Apr. 2013.

[20] S. Mukherjee, F. Libisch, N. Large, O. Neumann, L. V Brown, J. Cheng, J. B. Lassiter, E. A. Carter, P. Nordlander, and N. J. Halas, "Hot Electrons Do the Impossible: Plasmon-Induced Dissociation of H2 on Au," *Nano Lett.*, vol. 13, no. 1, pp. 240–247, 2013.

[21] K. Appavoo, B. Wang, N. F. Brady, M. Seo, J. Nag, R. P. Prasankumar, D. J. Hilton, S. T. Pantelides, and R. F. Haglund, "Ultrafast Phase Transition via Catastrophic Phonon Collapse Driven by Plasmonic Hot-Electron Injection," *Nano Lett.*, vol. 14, no. 3, pp. 1127–1133, Mar. 2014.

[22] Y. Kang, S. Najmaei, Z. Liu, Y. Bao, Y. Wang, X. Zhu, N. J. Halas, P. Nordlander, P. M. Ajayan, J. Lou, and Z. Fang, "Plasmonic Hot Electron Induced Structural Phase Transition in a MoS2 Monolayer," *Adv. Mater.*, vol. 26, no. 37, pp. 6467–6471, Aug. 2014.

[23] M. W. Knight, H. Sobhani, P. Nordlander, and N. J. Halas, "Photodetection with Active Optical Antennas," *Science (80-.).*, vol. 332, no. May, pp. 702–704, 2011.

[24] W. Li and J. Valentine, "Metamaterial Perfect Absorber Based Hot Electron

Photodetection," *Nano Lett.*, vol. 14, no. 6, pp. 3510–3514, 2014.

[25] H. Chalabi, D. Schoen, and M. L. Brongersma, "Hot-Electron Photodetection with a Plasmonic Nanostripe Antenna," *Nano Lett.*, vol. 14, no. 3, pp. 1374–1380, Feb. 2014.

[26] R. H. Fowler, "The Analysis of Photoelectric Sensitivity Curves for Clean Metals at Various Temperatures," *Physic Rev.*, vol. 38, no. 1, pp. 45–56, 1931.

[27] M. W. Knight, H. Sobhani, P. Nordlander, and N. J. Halas, "Photodetection with active optical antennas," *Science (80-.).*, vol. 332, no. 6030, pp. 702–4, May 2011.

[28] A. Giugni, B. Torre, A. Toma, M. Francardi, M. Malerba, A. Alabastri, R. Proietti Zaccaria, M. I. Stockman, and E. Di Fabrizio, "Hot-electron nanoscopy using adiabatic compression of surface plasmons," *Nat. Nanotechnol.*, vol. 8, no. 11, pp. 845–852, Nov. 2013.

[29] I. Goykhman, B. Desiatov, J. Khurgin, J. Shappir, and U. Levy, "Waveguide based compact silicon Schottky photodetector with enhanced responsivity in the telecom spectral band," *Opt. Express*, vol. 20, no. 27, pp. 28594–28602, Dec. 2012.

[30] W. Li and J. Valentine, "Metamaterial Perfect Absorber Based Hot Electron Photodetection," *Nano Lett.*, vol. 14, no. 6, pp. 3510–3514, Jun. 2014.

[31] Q. Xu, B. Schmidt, S. Pradhan, and M. Lipson, "Micrometre-scale silicon electro-optic modulator," *Nature*, vol. 435, no. 7040, pp. 325–327, May 2005.

[32] K. De Vos, I. Bartolozzi, E. Schacht, P. Bienstman, and R. Baets, "Silicon-on-Insulator microring resonator for sensitive and label-free biosensing," *Opt. Express*, vol. 15, no. 12, pp. 7610–7615, Jun. 2007.

[33] J. B. Khurgin and G. Sun, "Comparative analysis of spasers, vertical-cavity surface-emitting lasers and surface-plasmon-emitting diodes," *Nat Phot.*, vol. 8, no. 6, pp. 468–473, Jun. 2014.

[34] H. Altug, D. Englund, and J. Vuckovic, "Ultrafast photonic crystal nanocavity laser," *Nat Phys*, vol. 2, no. 7, pp. 484–488, Jul. 2006.

[35] U. P. Dharanipathy, M. Minkov, M. Tonin, V. Savona, and R. Houdré, "High-Q silicon photonic crystal cavity for enhanced optical nonlinearities," *Appl. Phys. Lett.*, vol. 105, no. 10, 2014.

[36] C. Kang, S. M. Weiss, Y. A. Vlasov, and S. Assef, "Optimized light–matter interaction and defect hole placement in photonic crystal cavity sensors," *Opt. Lett.*, vol. 37, no. 14, p. 2850, 2012.

[37] Y. Yang, W. Wang, A. Boulesbaa, I. I. Kravchenko, D. P. Briggs, A. Puretzky, D. Geohegan, and J. Valentine, "Nonlinear Fano-Resonant Dielectric Metasurfaces,"

Nano Lett., vol. 15, no. 11, pp. 7388–7393, Nov. 2015.

[38] Q. H. Wang, K. Kalantar-Zadeh, A. Kis, J. N. Coleman, and M. S. Strano, "Electronics and optoelectronics of two-dimensional transition metal dichalcogenides," *Nat. Nanotechnol.*, vol. 7, no. 11, pp. 699–712, Nov. 2012.

[39] K. S. Novoselov, D. Jiang, F. Schedin, T. J. Booth, V. V Khotkevich, S. V Morozov, and a K. Geim, "Two-dimensional atomic crystals," *Proc. Natl. Acad. Sci. U. S. A.*, vol. 102, no. 30, pp. 10451–3, Jul. 2005.

[40] S. Das Sarma, S. Adam, E. H. Hwang, and E. Rossi, "Electronic transport in two-dimensional graphene," *Rev. Mod. Phys.*, vol. 83, no. 2, pp. 407–470, May 2011.

[41] K. I. Bolotin, K. J. Sikes, Z. Jiang, M. Klima, G. Fudenberg, J. Hone, P. Kim, and H. L. Stormer, "Ultrahigh electron mobility in suspended graphene," *Solid State Commun.*, vol. 146, no. 9–10, pp. 351–355, Jun. 2008.

[42] Z. Q. Li, E. a. Henriksen, Z. Jiang, Z. Hao, M. C. Martin, P. Kim, H. L. Stormer, and D. N. Basov, "Dirac charge dynamics in graphene by infrared spectroscopy," *Nat. Phys.*, vol. 4, no. 7, pp. 532–535, Jun. 2008.

[43] R. R. Nair, P. Blake, A. N. Grigorenko, K. S. Novoselov, T. J. Booth, T. Stauber, N. M. R. Peres, and A. K. Geim, "Fine structure constant defines visual transparency of graphene," *Science*, vol. 320, no. June, p. 1308, 2008.

[44] L. a Falkovsky, "Optical properties of graphene," *J. Phys. Conf. Ser.*, vol. 129, p. 012004, Oct. 2008.

[45] F. Xia, H. Yan, and P. Avouris, "The Interaction of Light and Graphene: Basics, Devices, and Applications," *Proc. IEEE*, vol. 101, no. 7, pp. 1717–1731, Jul. 2013.

[46] L. Ju, B. Geng, J. Horng, C. Girit, M. Martin, Z. Hao, H. A. Bechtel, X. Liang, A. Zettl, Y. R. Shen, and F. Wang, "Graphene plasmonics for tunable terahertz metamaterials," *Nat Nano*, vol. 6, no. 10, pp. 630–634, Oct. 2011.

[47] A. N. Grigorenko, M. Polini, and K. S. Novoselov, "Graphene plasmonics," *Nat Phot.*, vol. 6, no. 11, pp. 749–758, Nov. 2012.

[48] F. Xia, H. Wang, D. Xiao, M. Dubey, and A. Ramasubramaniam, "Two-dimensional material nanophotonics," *Nat Phot.*, vol. 8, no. 12, pp. 899–907, Dec. 2014.

[49] K. F. Mak, C. Lee, J. Hone, J. Shan, and T. F. Heinz, "Atomically Thin MoS2: A New Direct-Gap Semiconductor," *Phys. Rev. Lett.*, vol. 105, no. 13, p. 136805, Sep. 2010.

[50] A. Kuc, N. Zibouche, and T. Heine, "Influence of quantum confinement on the electronic structure of the transition metal sulfide TS{}_{2}," *Phys. Rev. B*, vol. 83,

no. 24, p. 245213, Jun. 2011.

[51] M. Amani, D.-H. Lien, D. Kiriya, J. Xiao, A. Azcatl, J. Noh, S. R. Madhvapathy, R. Addou, S. KC, M. Dubey, K. Cho, R. M. Wallace, S.-C. Lee, J.-H. He, J. W. Ager, X. Zhang, E. Yablonovitch, and A. Javey, "Near-unity photoluminescence quantum yield in MoS2," *Science (80-.).*, vol. 350, no. 6264, pp. 1065–1068, Nov. 2015.

[52] J. C. Reed, A. Y. Zhu, H. Zhu, F. Yi, and E. Cubukcu, "Wavelength Tunable Microdisk Cavity Light Source with a Chemically Enhanced MoS2 Emitter," *Nano Lett.*, vol. 15, no. 3, pp. 1967–1971, Mar. 2015.

[53] A. K. M. Newaz, D. Prasai, J. I. Ziegler, D. Caudel, S. Robinson, R. F. Haglund Jr., and K. I. Bolotin, "Electrical control of optical properties of monolayer MoS2," *Solid State Commun.*, vol. 155, pp. 49–52, Feb. 2013.

[54] H. J. Conley, B. Wang, J. I. Ziegler, R. F. Haglund, S. T. Pantelides, and K. I. Bolotin, "Bandgap Engineering of Strained Monolayer and Bilayer MoS2," *Nano Lett.*, vol. 13, no. 8, pp. 3626–3630, Aug. 2013.

[55] H. S. Lee, S.-W. Min, Y.-G. Chang, M. K. Park, T. Nam, H. Kim, J. H. Kim, S. Ryu, and S. Im, "MoS2 Nanosheet Phototransistors with Thickness-Modulated Optical Energy Gap," *Nano Lett.*, vol. 12, no. 7, pp. 3695–3700, Jul. 2012.

[56] Z. Ma, Z. Li, K. Liu, C. Ye, and V. J. Sorger, "Indium-Tin-Oxide for High-performance Electro-optic Modulation," *Nanophotonics*, vol. 4, no. 1, pp. 198–213, 2015.

[57] J. Yoon, M. Zhou, M. A. Badsha, T. Y. Kim, Y. C. Jun, and C. K. Hwangbo, "Broadband Epsilon-Near-Zero Perfect Absorption in the Near-Infrared," *Sci. Rep.*, vol. 5, p. 12788, Aug. 2015.

[58] E. Feigenbaum, K. Diest, and H. A. Atwater, "Unity-Order Index Change in Transparent Conducting Oxides at Visible Frequencies," *Nano Lett.*, vol. 10, no. 6, pp. 2111–2116, Jun. 2010.

[59] A. Melikyan, N. Lindenmann, S. Walheim, P. M. Leufke, S. Ulrich, J. Ye, P. Vincze, H. Hahn, T. Schimmel, C. Koos, W. Freude, and J. Leuthold, "Surface plasmon polariton absorption modulator," *Opt. Express*, vol. 19, no. 9, pp. 8855–8869, Apr. 2011.

[60] X. Gan, R.-J. Shiue, Y. Gao, I. Meric, T. F. Heinz, K. Shepard, J. Hone, S. Assefa, and D. Englund, "Chip-integrated ultrafast graphene photodetector with high responsivity," *Nat Phot.*, vol. 7, no. 11, pp. 883–887, Nov. 2013.

[61] C.-H. Liu, Y.-C. Chang, T. B. Norris, and Z. Zhong, "Graphene photodetectors with ultra-broadband and high responsivity at room temperature," *Nat Nano*, vol. 9, no. 4, pp. 273–278, Apr. 2014.

[62] B. Y. Zhang, T. Liu, B. Meng, X. Li, G. Liang, X. Hu, and Q. J. Wang, "Broadband high photoresponse from pure monolayer graphene photodetector," *Nat Commun*, vol. 4, p. 1811, May 2013.

[63] A. Pospischil, M. Humer, M. M. Furchi, D. Bachmann, R. Guider, T. Fromherz, and T. Mueller, "CMOS-compatible graphene photodetector covering all optical communication bands," *Nat Phot.*, vol. 7, no. 11, pp. 892–896, Nov. 2013.

[64] F. Xia, T. Mueller, Y. Lin, A. Valdes-Garcia, and P. Avouris, "Ultrafast graphene photodetector," *Nat Nano*, vol. 4, no. 12, pp. 839–843, Dec. 2009.

[65] A. Urich, K. Unterrainer, and T. Mueller, "Intrinsic response time of graphene photodetectors," *Nano Lett.*, vol. 11, no. 7, pp. 2804–2808, Jul. 2011.

[66] F. H. L. Koppens, T. Mueller, P. Avouris, A. C. Ferrari, M. S. Vitiello, and M. Polini, "Photodetectors based on graphene, other two-dimensional materials and hybrid systems," *Nat Nano*, vol. 9, no. 10, pp. 780–793, Oct. 2014.

[67] T. Mueller, F. Xia, M. Freitag, J. Tsang, and P. Avouris, "Role of contacts in graphene transistors: A scanning photocurrent study," *Phys. Rev. B*, vol. 79, no. 24, p. 245430, Jun. 2009.

[68] T. Mueller, F. Xia, and P. Avouris, "Graphene photodetectors for high-speed optical communications," *Nat. Photonics*, vol. 4, no. 5, pp. 297–301, 2010.

[69] RadisavljevicB., RadenovicA., BrivioJ., GiacomettiV., and KisA., "Single-layer MoS2 transistors," *Nat Nano*, vol. 6, no. 3, pp. 147–150, Mar. 2011.

[70] O. Lopez-Sanchez, D. Lembke, M. Kayci, A. Radenovic, and K. Andras, "Ultrasensitive photodetectors based on monolayer MoS2," *Nat. Nanotechnol.*, vol. 8, no. 7, pp. 497–501, Jul. 2013.

[71] A. R. Klots, A. K. M. Newaz, B. Wang, D. Prasai, H. Krzyzanowska, J. Lin, D. Caudel, N. J. Ghimire, J. Yan, B. L. Ivanov, K. A. Velizhanin, A. Burger, D. G. Mandrus, N. H. Tolk, S. T. Pantelides, and K. I. Bolotin, "Probing excitonic states in suspended two-dimensional semiconductors by photocurrent spectroscopy," *Sci. Rep.*, vol. 4, p. 6608, Oct. 2014.

[72] K. Roy, M. Padmanabhan, S. Goswami, T. P. Sai, G. Ramalingam, S. Raghavan, and A. Ghosh, "Graphene-MoS2 hybrid structures for multifunctional photoresponsive memory devices," *Nat Nano*, vol. 8, no. 11, pp. 826–830, Nov. 2013.

[73] W. J. Yu, Y. Liu, H. Zhou, A. Yin, Z. Li, Y. Huang, and X. Duan, "Highly efficient gate-tunable photocurrent generation in vertical heterostructures of layered materials," *Nat. Nanotechnol.*, vol. 8, no. 12, pp. 952–958, Dec. 2013.

[74] L. Britnell, R. M. Ribeiro, A. Eckmann, R. Jalil, B. D. Belle, A. Mishchenko, Y.-J.

Kim, R. V Gorbachev, T. Georgiou, S. V Morozov, A. N. Grigorenko, A. K. Geim, C. Casiraghi, A. H. C. Neto, and K. S. Novoselov, "Strong Light-Matter Interactions in Heterostructures of Atomically Thin Films," *Science (80-.).*, vol. 340, no. 6138, pp. 1311–1314, Jun. 2013.

[75] M. A. Kats, R. Blanchard, P. Genevet, Z. Yang, M. M. Qazilbash, D. N. Basov, S. Ramanathan, and F. Capasso, "Thermal tuning of mid-infrared plasmonic antenna arrays using a phase change material," *Opt. Lett.*, vol. 38, no. 3, pp. 368–370, 2013.

[76] N. I. Zheludev and E. Plum, "Reconfigurable nanomechanical photonic metamaterials," *Nat Nano*, vol. 11, no. 1, pp. 16–22, Jan. 2016.

[77] D. Pacifici, H. J. Lezec, and H. A. Atwater, "All-optical modulation by plasmonic excitation of CdSe quantum dots," *Nat Phot.*, vol. 1, no. 7, pp. 402–406, Jul. 2007.

[78] C. T. Phare, Y.-H. Daniel Lee, J. Cardenas, and M. Lipson, "Graphene electro-optic modulator with 30 GHz bandwidth," *Nat Phot.*, vol. 9, no. 8, pp. 511–514, Aug. 2015.

[79] M. Liu, X. Yin, E. Ulin-Avila, B. Geng, T. Zentgraf, L. Ju, F. Wang, and X. Zhang, "A graphene-based broadband optical modulator," *Nature*, vol. 474, no. 7349, pp. 64–7, Jun. 2011.

[80] J. Park, J.-H. Kang, X. Liu, and M. L. Brongersma, "Electrically Tunable Epsilon-Near-Zero (ENZ) Metafilm Absorbers," *Sci. Rep.*, vol. 5, p. 15754, Nov. 2015.

[81] Sorger Volker J, L.-K. N. D, M. Ren-Min, and Z. Xiang, "Ultra-compact silicon nanophotonic modulator with broadband response," *Nanophotonics*, vol. 1. p. 17, 2012.

[82] A. V Krasavin and A. V Zayats, "Photonic Signal Processing on Electronic Scales: Electro-Optical Field-Effect Nanoplasmonic Modulator," *Phys. Rev. Lett.*, vol. 109, no. 5, p. 53901, Jul. 2012.

[83] a. K. M. Newaz, D. Prasai, J. I. Ziegler, D. Caudel, S. Robinson, R. F. Haglund Jr., and K. I. Bolotin, "Electrical control of optical properties of monolayer MoS2," *Solid State Commun.*, vol. 155, pp. 49–52, Feb. 2013.

[84] X. Hong, J. Kim, S.-F. Shi, Y. Zhang, C. Jin, Y. Sun, S. Tongay, J. Wu, Y. Zhang, and F. Wang, "Ultrafast charge transfer in atomically thin MoS2/WS2 heterostructures," *Nat Nano*, vol. 9, no. 9, pp. 682–686, Sep. 2014.

[85] T. Cheiwchanchamnangij and W. R. L. Lambrecht, "Quasiparticle band structure calculation of monolayer, bilayer, and bulk MoS2," *Phys. Rev. B*, vol. 85, no. 20, p. 205302, May 2012.

[86] Y. Tan, R. He, C. Cheng, D. Wang, Y. Chen, and F. Chen, "Polarization-dependent optical absorption of MoS2 for refractive index sensing," *Sci. Rep.*, vol.

4, p. 7523, Jan. 2014.

[87] T. J. Echtermeyer, L. Britnell, P. K. Jasnos, A. Lombardo, R. V Gorbachev, A. N. Grigorenko, A. K. Geim, A. C. Ferrari, and K. S. Novoselov, "Strong plasmonic enhancement of photovoltage in graphene," *Nat Commun*, vol. 2, p. 458, Aug. 2011.

[88] M. Furchi, A. Urich, A. Pospischil, G. Lilley, K. Unterrainer, H. Detz, P. Klang, A. M. Andrews, W. Schrenk, G. Strasser, and T. Mueller, "Microcavity-integrated graphene photodetector," *Nano Lett.*, vol. 12, no. 6, pp. 2773–2777, Jun. 2012.

[89] N. M. Gabor, J. C. W. Song, Q. Ma, N. L. Nair, T. Taychatanapat, K. Watanabe, T. Taniguchi, L. S. Levitov, and P. Jarillo-Herrero, "Hot carrier-assisted intrinsic photoresponse in graphene," *Science (80-.).*, vol. 334, no. 6056, pp. 648–52, Nov. 2011.

[90] U. Fano, "Effects of Configuration Interaction on Intensities and Phase Shifts," *Phys. Rev.*, vol. 124, no. 6, pp. 1866–1878, 1961.

[91] S. Fan, W. Suh, and J. D. Joannopoulos, "Temporal coupled-mode theory for the Fano resonance in optical resonators," *J. Opt. Soc. Am. A*, vol. 20, no. 3, pp. 569–572, 2003.

[92] S. Fan and J. Joannopoulos, "Analysis of guided resonances in photonic crystal slabs," *Phys. Rev. B*, vol. 65, no. 23, p. 235112, Jun. 2002.

[93] J. D. Joannopoulos, S. G. Johnson, J. N. Winn, and R. D. Meade, *Photonic Crystals: Molding the Flow of Light*, 2nd ed. Princeton University Press, 2008.

[94] M. Freitag, M. Steiner, Y. Martin, V. Perebeinos, Z. Chen, J. C. Tsang, and P. Avouris, "Energy dissipation in graphene field-effect transistors," *Nano Lett.*, vol. 9, no. 5, pp. 1883–1888, May 2009.

[95] R. N. Zitter, "Saturated Optical Absorption Through Band Filling in Semiconductors," *Appl. Phys. Lett.*, vol. 14, no. 2, p. 73, 1969.

[96] M. Freitag, T. Low, F. Xia, and P. Avouris, "Photoconductivity of biased graphene," *Nat. Photonics*, vol. 7, no. 1, pp. 53–59, Dec. 2013.

[97] J. C. W. Song, M. S. Rudner, C. M. Marcus, and L. S. Levitov, "Hot Carrier Transport and Photocurrent Response in Graphene," *Nano Lett.*, vol. 11, no. 11, pp. 4688–4692, May 2011.

[98] X. Xu, N. M. Gabor, J. S. Alden, A. van der Zande, and P. L. McEuen, "Photo-Thermoelectric Effect at a Graphene Interface Junction," *Nano Lett.*, vol. 10, no. 2, pp. 562–566, Jul. 2010.

[99] K. Appavoo and R. F. Haglund Jr., "Polarization selective phase-change

nanomodulator," *Sci. Rep.*, vol. 4, p. 6771, Oct. 2014.

[100] M. Liu, X. Yin, E. Ulin-Avila, B. Geng, T. Zentgraf, L. Ju, F. Wang, and X. Zhang, "A graphene-based broadband optical modulator," *Nature*, vol. 474, no. 7349, pp. 64–67, Jun. 2011.

[101] D. Pacifici, H. J. Lezec, and H. A. Atwater, "All-optical Modulation by Plasmonic Excitation of CdSe Quantum Dots," *Nat. Photonics*, vol. 1, pp. 402–407, 2007.

[102] Z. Miao, Q. Wu, X. Li, Q. He, K. Ding, Z. An, Y. Zhang, and L. Zhou, "Full-range Gate-controlled Terahertz Phase Modulation with Graphene Metasurfaces," in *CLEO: 2015*, 2015, p. AF2E.6.

[103] Y. Yao, R. Shankar, M. A. Kats, Y. Song, J. Kong, M. Loncar, and F. Capasso, "Electrically Tunable Metasurface Perfect Absorbers for Ultrathin Mid-Infrared Optical Modulators," *Nano Lett.*, vol. 14, no. 11, pp. 6526–6532, Nov. 2014.

[104] S.-F. Shi, B. Zeng, H.-L. Han, X. Hong, H.-Z. Tsai, H. S. Jung, A. Zettl, M. F. Crommie, and F. Wang, "Optimizing Broadband Terahertz Modulation with Hybrid Graphene/Metasurface Structures," *Nano Lett.*, vol. 15, no. 1, pp. 372–377, Jan. 2015.

[105] S. Vassant, A. Archambault, F. Marquier, F. Pardo, U. Gennser, A. Cavanna, J. L. Pelouard, and J. J. Greffet, "Epsilon-Near-Zero Mode for Active Optoelectronic Devices," *Phys. Rev. Lett.*, vol. 109, no. 23, p. 237401, Dec. 2012.

[106] S. Jahani and Z. Jacob, "All-dielectric metamaterials," *Nat Nano*, vol. 11, no. 1, pp. 23–36, Jan. 2016.

[107] C. Huygens, *Traité de la Lumière*. Leyden: Pieter van der Aa, 1690.

[108] A. E. H. Love, "The Integration of the Equations of Propagation of Electric Waves," *Philos. Trans. R. Soc. London A Math. Phys. Eng. Sci.*, vol. 197, no. 287–299, pp. 1–45, 1901.

[109] C. Pfeiffer and A. Grbic, "Metamaterial Huygens' Surfaces: Tailoring Wave Fronts with Reflectionless Sheets," *Phys. Rev. Lett.*, vol. 110, no. 19, p. 197401, May 2013.

[110] F. Monticone, N. M. Estakhri, and A. Alu, "Full Control of Nanoscale Optical Transmission with a Composite Metascreen," *Phys. Rev. Lett.*, vol. 110, p. 203903, 2013.

[111] M. Decker, I. Staude, M. Falkner, J. Dominguez, D. N. Neshev, I. Brener, T. Pertsch, and Y. S. Kivshar, "High-Efficiency Dielectric Huygens' Surfaces," *Adv. Opt. Mater.*, vol. 3, no. 6, pp. 813–820, 2015.

[112] S. Campione, I. Brener, and F. Marquier, "Theory of epsilon-near-zero modes in

ultrathin films," *Phys. Rev. B*, vol. 91, no. 12, p. 121408, Mar. 2015.

[113] G. Khitrova, H. M. Gibbs, M. Kira, S. W. Koch, and A. Scherer, "Vacuum Rabi splitting in semiconductors," *Nat Phys*, vol. 2, no. 2, pp. 81–90, Feb. 2006.

[114] Y. C. Jun, J. Reno, T. Ribaudo, E. Shaner, J.-J. Greffet, S. Vassant, F. Marquier, M. Sinclair, and I. Brener, "Epsilon-Near-Zero Strong Coupling in Metamaterial-Semiconductor Hybrid Structures," *Nano Lett.*, vol. 13, no. 11, pp. 5391–5396, Nov. 2013.

[115] D. Prasai, A. Klots, A. Newaz, J. S. Niezgoda, N. Orfield, C. Escobar, A. Wynn, A. Efimov, G. K. Jennings, S. J. Rosenthal, and K. Bolotin, "Electrical control of near-field energy transfer between quantum dots and 2D semiconductors," *Nano Lett.*, vol. 15, no. 7, pp. 4347–4380, Jun. 2015.

[116] R. Sundararaman, P. Narang, A. S. Jermyn, W. a. Goddard III, and H. a. Atwater, "Theoretical predictions for hot-carrier generation from surface plasmon decay," *Nat. Commun.*, vol. 5, p. 5788, Dec. 2014.

[117] C. Clavero, "Plasmon-induced hot-electron generation at nanoparticle/metal-oxide interfaces for photovoltaic and photocatalytic devices," *Nat Phot.*, vol. 8, no. 2, pp. 95–103, Feb. 2014.

[118] M. L. Brongersma, N. J. Halas, and P. Nordlander, "Plasmon-induced hot carrier science and technology," *Nat. Nanotechnol.*, vol. 10, no. 1, pp. 25–34, Jan. 2015.

[119] B. Y. Zheng, Y. Wang, P. Nordlander, and N. J. Halas, "Color-selective and CMOS-compatible photodetection based on aluminum plasmonics," *Adv. Mater.*, vol. 26, no. 36, pp. 6318–23, Sep. 2014.

[120] C. Clavero, "Plasmon-induced hot-electron generation at nanoparticle/metal-oxide interfaces for photovoltaic and photocatalytic devices," *Nat. Photonics*, vol. 8, no. 2, pp. 95–103, Jan. 2014.

[121] Z. Fang, Y. Wang, Z. Liu, A. Schlather, P. M. Ajayan, F. H. L. Koppens, P. Nordlander, and N. J. Halas, "Plasmon-induced doping of graphene," *ACS Nano*, vol. 6, no. 11, pp. 10222–10228, Nov. 2012.

[122] T. Hong, B. Chamlagain, S. Hu, S. M. Weiss, Z. Zhou, and Y. Xu, "Plasmonic Hot Electron Induced Photocurrent Response at MoS2-Metal Junctions," *ACS Nano*, vol. 9, no. 5, pp. 5357–5363, 2015.

[123] Z. Fang, Y. Wang, Z. Liu, A. Schlather, P. M. Ajayan, F. H. L. Koppens, P. Nordlander, and N. J. Halas, "Plasmon-Induced Doping of Graphene," *ACS Nano*, vol. 6, no. 11, pp. 10222–10228, Nov. 2012.

[124] S. Ghatak, A. N. Pal, and A. Ghosh, "Nature of Electronic States in Atomically Thin MoS2 Field-Effect Transistors," *ACS Nano*, vol. 5, no. 10, pp. 7707–7712,

2011.

[125] M. Buscema, M. Barkelid, V. Zwiller, H. S. J. Van Der Zant, G. A. Steele, and A. Castellanos-gomez, "Large and Tunable Photothermoelectric Effect in Single-Layer MoS2," *Nano Lett.*, vol. 13, no. 2, pp. 358–363, 2013.

[126] Y. Zhang, H. Li, L. Wang, H. Wang, X. Xie, S.-L. Zhang, R. Liu, and Z.-J. Qiu, "Photothermoelectric and photovoltaic effects both present in MoS2," *Sci. Rep.*, vol. 5, p. 7938, Jan. 2015.

[127] P. J. Zomer, S. P. Dash, N. Tombros, and B. J. van Wees, "A transfer technique for high mobility graphene devices on commercially available hexagonal boron nitride," *Appl. Phys. Lett.*, vol. 99, no. 23, p. 232104, 2011.

[128] S. Bertolazzi, J. Brivio, and A. Kis, "Stretching and Breaking of Ultrathin MoS2," *ACS Nano*, vol. 5, no. 12, pp. 9703–9709, 2011.

[129] K. K. Sze, S. M.; Ng, *Physics of Semiconductor Devices*, 3rd ed. Hoboken, NJ: John Wiley & Sons, Inc., 2007.

[130] H. Zhong, Z. Ni, Y. Wang, M. Ye, Z. Song, Y. Pan, R. Quhe, J. Yang, L. Yang, J. Shi, and J. Lu, "Interfacial Properties of Monolayer and Bilayer MoS 2 Contacts with Metals : Depressed Many-electron Effects," *arXiv Prepr. arXiv1501.01071*, 2015.

[131] M. Bernardi, J. Mustafa, J. B. Neaton, and S. G. Louie, "Theory and computation of hot carriers generated by surface plasmon polaritons in noble metals," *Nat. Commun.*, vol. 6, p. 7044, Jun. 2015.

[132] K.-T. Lin, H.-L. Chen, Y.-S. Lai, and C.-C. Yu, "Silicon-based broadband antenna for high responsivity and polarization-insensitive photodetection at telecommunication wavelengths," *Nat. Commun.*, vol. 5, p. 3288, Jan. 2014.

[133] H. S. Lee, S. Min, Y. Chang, M. K. Park, T. Nam, H. Kim, J. H. Kim, S. Ryu, and S. Im, "MoS2 Nanosheet Phototransistors with Thickness-Modulated Optical Energy Gap," *Nano Lett.*, vol. 12, no. 7, p. 3695−3700, 2012.

[134] K. Roy, M. Padmanabhan, S. Goswami, T. P. Sai, G. Ramalingam, S. Raghavan, and A. Ghosh, "Graphene-MoS2 hybrid structures for multifunctional photoresponsive memory devices," *Nat. Nanotechnol.*, vol. 8, no. 11, pp. 826–830, Nov. 2013.

[135] M. Kan, J. Y. Wang, X. W. Li, S. H. Zhang, Y. W. Li, Y. Kawazoe, Q. Sun, and P. Jena, "Structures and Phase Transition of a MoS2 Monolayer," *J. Phys. Chem. C*, vol. 118, no. 3, pp. 1515–1522, 2014.

[136] G. V Naik and J. A. Dionne, "Photon upconversion with hot carriers in plasmonic systems," *Appl. Phys. Lett.*, vol. 107, no. 13, 2015.

[137] C. Lee, H. Yan, L. E. Brus, T. F. Heinz, J. Hone, and S. Ryu, "Anomalous Lattice Vibrations of Single- and Few-Layer MoS2," *ACS Nano*, vol. 4, no. 5, pp. 2695–2700, 2010.